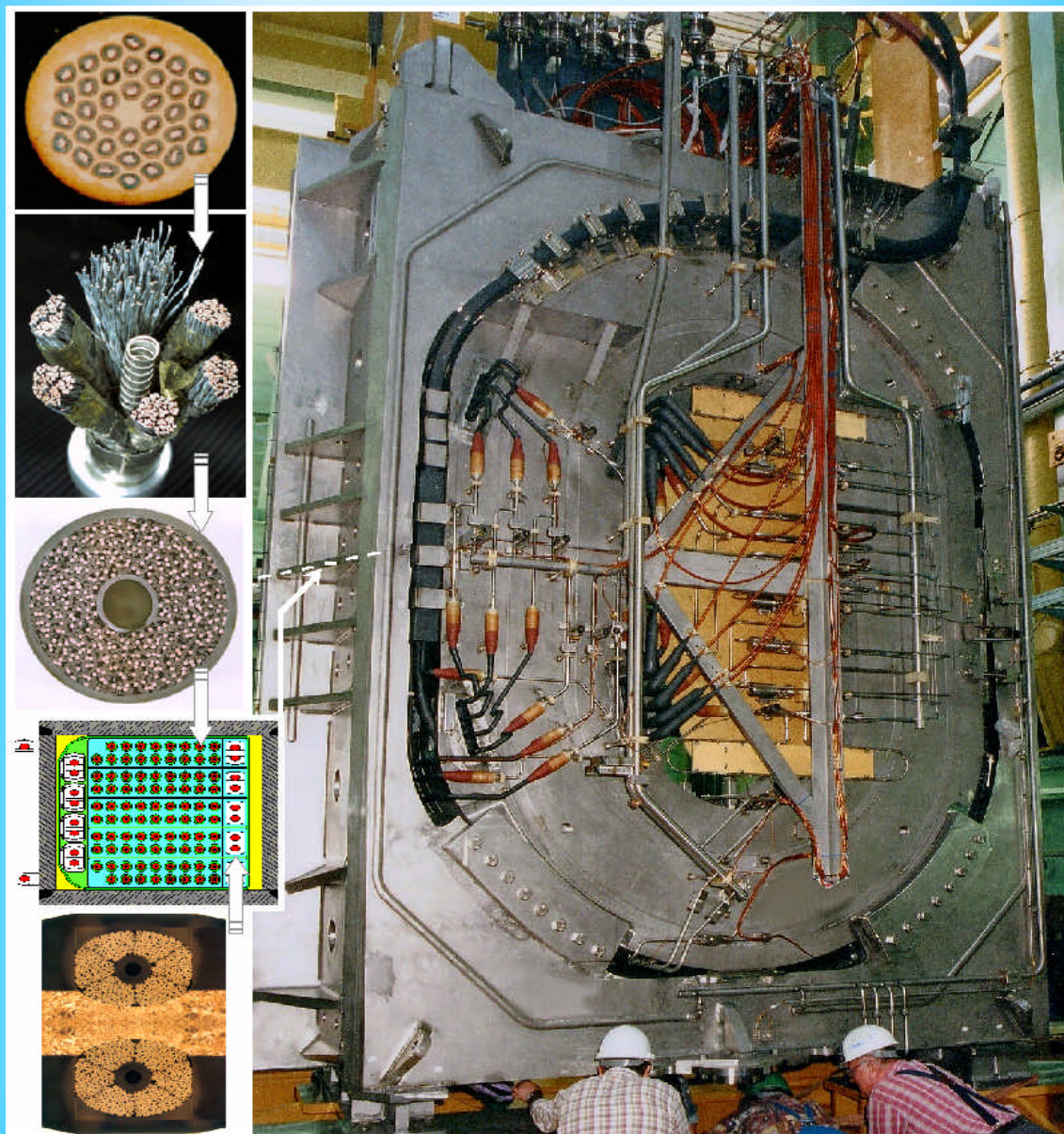


FUSION TECHNOLOGY

Annual Report of the Association EURATOM/CEA 2001

Compiled by : Ph. MAGAUD and F. Le VAGUERES



ASSOCIATION EURATOM/CEA
DSM/DRFC
CEA/CADARACHE
13108 Saint-Paul-Lez-Durance (France)

FUSION TECHNOLOGY

Annual Report of the Association CEA/EURATOM 2001

Compiled by : Ph. MAGAUD and F. LE VAGUERES

ASSOCIATION CEA/EURATOM
DSM/DRFC
CEA CADARACHE
13108 Saint-Paul-Lez-Durance (France)

Tél. : 33 - 4 42 25 46 59
Fax : 33 - 4 42 25 64 21
e-mail : dirdrfc@drfc.cad.cea.fr
Web : <http://www-fusion-magnetique.cea.fr>

This report is also available on-line at : <http://www-fusion-magnetique.cea.fr>

1	6
2	
3	
4	
5	

Cover : Toroidal Field Model Coil (TFMC) installation and test

- 1 – Superconducting strand (courtesy of ENEA)
- 2&3 – Superconducting conductor (courtesy of ENEA)
- 4 – Cross section of the TMFC
- 5 – Superconducting joint
- 6 – TFMC at FZK (courtesy of FZK)

CONTENTS

<i>INTRODUCTION</i>	1
---------------------------	---

<i>EFDA TECHNOLOGY PROGRAMME</i>	3
--	---

Physics Integration

Diagnostics

CEFDA00-561	Support to ITER diagnostic design : polarimetry	5
TW0-DIAG-DEV	ITER diagnostic window development	7

Heating and Current Drive

CEFDA00-553	Support to ITER-FEAT lower hybrid launcher and transmission line	11
CEFDA00-546	Support to ITER ICRF system physics and engineering design - Electrical design of an ICRF array for high RF power density in ITER-FEAT	15
CEFDA00-569	Development of vacuum coaxial capacitors for the ITER-like ICRF JET antenna	19
TW0-ICRF/ANT	ICRF Antenna and vacuum transmission line development - ICRH Antenna coupling : near field computations part II	23
TW1-TPH-ICRANT	ICRF Antenna and vacuum transmission line development - Design & manufacturing of a CW ICRF high power test rig and testing of next step antenna prototype components	29
TW0-NB.DEV.1	Neutral beam development for EDA extension - EU-JA collaborative experiment on KAMABOKO source	31

Vessel/In Vessel

Plasma Facing Components

CNET98-480	Thermal fatigue testing of divertor full scale prototype - 200 kW electron beam gun test	35
CNET98-485	Thermal fatigue testing of baffle full scale prototype - 200 kW electron beam gun test	39
CEFDA00-543	High heat flux testing and analysis of small scale mock-ups - Part 2 : Analysis	43
CEFDA00-565	Improvement evaluation for infrared detection of PFC defects - SATIR upgrading	47
CEFDA01-581	Critical heat flux testing of hypervaportrons - 200 kW electron beam gun test	51

DV4.3	Optimisation and manufacture of high heat flux components - Study of flat tile cascade failure possibility for high heat flux components	53
TW0-DV4/01	Optimisation of manufacture of high heat flux components : tungsten monoblocks	55
TW0-T438-01	Development and testing of time resolved erosion detecting techniques	59
TW1-TVP-MAN1	Optimisation and testing optimisation of CuCrZr/SS tube joints - Optimisation and manufacturing of samples by diffusion bonding	63
Vessel/Blanket		
CEFDA00-556	Simulation of ultrasonic inspection process	67
CEFDA01-587	Study to evaluate ITER proposals for VV code use	71
TW0-LASER/CUT	VV intersector maintenance - Further development of high power Nd YAG laser cutting - Improvement of YAG laser backplate cutting by adding powder ...	73
TW0-LASER/HYD	YAG laser process for cutting and welding of the blanket module hydraulic connections	77
TW0-LASER/REWELD	VV intersector maintenance - Further development of high power Nd - YAG laser rewelding after cutting	81
TW0-LASER/WELD	VV intersector joining - Further development of high power Nd - YAG laser welding with multipass filler wire	85
TW1-TVV-LWELD	VV intersector joining - Vacuum vessel laser assembly	87
T216-GB8	Small scale testing of first wall/shield modules	91
TW0-T420/06	Fabrication of a first wall panel with HIP'ed beryllium armor	93
TW0-T420/08	Development of HIP fabrication technique	99
TW0-T508/04	Development of Be/CuCrZr HIPping technique	103
TW0-T508/05	Development of Be/CuCrCz brazing technique	105
TW1-TVV-HIP	Improvement of HIP fabrication techniques	107
TW1-TVV-ONE	Optimisation of one step SS/SS and SS/CuCrZr HIP joints for retainment of CuCrZr properties	111
Remote Handling		
CEFDA00-524	Study to optimise intersector welding robot (IWR) design and machining characteristics	115
T252	Radiation tolerance assessment of standard components for remote handling and process instrumentation	119
T329-5	In-vessel RH dexterous operations - Task extension 2	125
TW0-DTP/1.1 TW1-TVA-BTS	Carrier and bore tools for 4" bent pipes	129
TW1-TVA-IVP TW0-DTP1.2&4	Prototypical manipulator for access through IVVS penetrations (IVP)	133

TW1-TVA-MANIP	In-vessel dexterous manipulator	137
TW1-TVA-RADTOL	Radiation tolerance assessment of remote handling components	139

Magnet Structure

Cryoplant

CEFDA00-517	Design of cryogenic transfer lines and ring manifolds for ITER-FEAT	143
CEFDA00-566	Layout of the cryoplant for RTO/RC ITER	145

Magnets

CEFDA00-541	Magnet design on PF and correction coils : conceptual design and analysis	147
M40	Design work on magnet R&D	153
M50	Conductor R&D - Development of NbTi conductors for ITER PF coils	157
TW0-T400/01	CSMC and TFMC installation and test	159
TW1-TMC-CODES	Design and interpretation codes	163
TW1-TMC-SCABLE	Cable and conductor characterization	167

Tritium Breeding and Materials

Breeding Blanket

Water Cooled Lithium Lead (WCLL) Blanket

TW1-TTBA-001-D01	Test blanket module - Adaptation to next step machine	169
TW1-TTBA-001-D04	Tritium breeding module adaptation to next step machine - Adaptation of thermal-hydraulic performance to ITER specification	173
TW1-TTBA-002-D01	Blanket manufacturing techniques - Definition of specification of a demonstrator	175
TTBA-2.1	Blanket manufacturing techniques - Definition of specifications for demonstrators	179
TTBA-2.2	Blanket manufacturing techniques - Solid HIP demonstrator for fabrication and coating, fabrication of double wall tubes	183
TW1-TTBA-002-D02	Blanket manufacturing techniques - Solid HIP demonstrator for fabrication and coating, fabrication of double wall tubes	185
TW1-TTBA-002-D03	Blanket manufacturing techniques - DIADEMO experimental program - Results of U bent DWT tests on Pb-Li	189
TW1-TTBA-002-D05	Blanket manufacturing techniques - Integrated mixed-powder HIP fabrication route for TBM with DWT	193
TTBA-3.5	Coating qualification and irradiation tests - Permeation out-of-pile testing	197
TW1-TTBA-004-D03	Processes and components - Blanket neutronic instrumentation	199

TW1-TTBA-005-D02	Safety and licensing : Pb-17Li/water interactions	201
TW1-TTBA-005-D03	Safety and licensing - TBM and TBM system safety	203
TW1-TTBA-006-D02	MHD effects - Test and modelling of natural MHD convection	209

Helium Cooled Pebble Bed (HCPB) Blanket

TW1-TTBB-002-D02	Blanket manufacturing techniques - Mock-up of first wall manufactured with alternative reduced cost fabrication technique	213
TTBB-2.3	Blanket manufacturing techniques - First wall manufacturing by HIP forming technique	217
TW1-TTBB-005-D03	Development of ceramic breeder pebble beds - Characterization of Li ₂ TiO ₃ pebble beds	219
TW1-TTBB-005-D04	Development of ceramic breeder pebble beds - Validation of Li ₂ TiO ₃ fabrication with pre-industrial means of the lab fabrication steps - Mastering/optimisation	223

Structural materials development

Advanced materials

TW1-TTMA-001-D01	SiC-SiC ceramic composite - SiC-SiC composite development and characterization	227
TW1-TTMA-001-D09	SiC-SiC ceramic composite - Joining development : process and mechanical characterization	231

Reduced Activation Ferritic Martensitic (RAFM) steels

TW1-TTMS-001-D02	RAFM steels - Irradiation performance - Neutron irradiation to 30-35 dpa at 325°C	235
TW1-TTMS-002-D03	RAFM steels - Metallurgical and mechanical characterization - Characterization and physical metallurgy	239
TW1-TTMS-002-D04	RAFM steels - Metallurgical and mechanical characterization - Thermal ageing behaviour of EUROFER 97	243
TW1-TTMS-002-D16	RAFM steels - Metallurgical and mechanical characterization - Mechanical properties of diffusion bonded welds (RAFM/RAFM HIP joint)	247
TW1-TTMS-002-D18	RAFM steels - Metallurgical and mechanical characterization - Mechanical properties of HIP powder steel	251
SM-3-3	Corrosion in water conditions (EUROFER 97 and F82H)	253
TW1-TTMS-003-D12	RAFM steels - Stress corrosion cracking in aqueous environments	257
TW1-TTMS-004-D02	RAFM steels - Qualification fabrication processes - Powder HIP processing & specification	259
SM-2-3-1	Mechanical properties of F82H weldments	263
TTMS-2.3.2	Mechanical properties of EUROFER 97 weldments	265
TW1-TTMS-004-D04	RAFM steels - Qualification fabrication processes - EUROFER weldability	267
TW1-TTMS-004-D05	RAFM steels - Qualification fabrication processes - Dissimilar welding with filler	271

TW1-TTMS-004-D06	RAFM steels - Qualification fabrication processes - Solid HIP process qualification, application to complex shapes	275
TW1-TTMS-005-D02	RAFM steels - Rules for design, fabrication and inspection - Design code assessment and development	279
TW1-TTMS-005-D05	RAFM steels - Rules for design, fabrication and inspection - RAFM data collection and data base maintenance	281
TW1-TTMS-006-D01	RAFM steels - Qualification of high performance steels - ODS process and qualification	283
TTMS-6.3.1 TW1-TTMS-006-D03	RAFM steels - Qualification of high performance steels - Microstructure and mechanical properties	287
Neutron source		
TTMI-001	IFMIF - Accelerator facility	291

Safety and Environment

SEA5-1	Validation of computer codes and models	295
SEA5-2	Coherent system of codes for the ITER safety analysis - Validation of computer codes and models	299
TSW-2.1	Waste and decommissioning strategy - Improvement to an existing facility and possibilities for diminishing gas release	301
TSW-2.6	Waste and decommissioning strategy - Requirements of decommissioning and waste management strategies	303
TW0-SEA4 SEA4-4	In-vessel safety - Third set of pre and post calculation of in-vessel LOCA's on the new japanese "ICE" facility	307
TW0-SEA3.5 TW1-TSS-SEA3.5	In-vessel hydrogen deflagration/detonation analysis	311
SEA5.31 TW1-TSS-SEA5	Validation of computer codes and models	313
TW1-TSS-SERF2	Tritium releases and long term impacts	315

System Studies

Power Plant Conceptual Studies (PPCS)

TW0-TRP-3D1	Analyze the sensitivity of achieving accident management	319
TW0-TRP-4D5	In-vessel components	321
TW1-TRP-PPCS1-D04	Model A (WCLL) - Consistency with the PPCS GDRD	325
TW1-TRP-PPCS1-D10	Model A (WCLL) - Design integration	327
TW1-TRP-PPCS3-D01	Selection of advanced models - Assessment of Pb-17Li cooled blanket and divertor concepts using SiC _f /SiC as structural material	331

Socio-economic studies

TW1-TRE-ECFA-D01	Externalities of fusion - Comparison of fusion external costs with advanced nuclear fission reactor	335
TW1-TRE-ECFA-D02	Externalities of fusion accident - Sensitivity analysis on plant model and site location	339

JET Technology

JET-EP-Div	The JET EP divertor project	343
JW0-FT-2.5	Tritium processes and waste management - Dedicated procedures for the detritiation of selected materials	347

<i>UNDERLYING TECHNOLOGY PROGRAMME</i>	349
---	-----

Physics Integration

Diagnostics

UT-PE-HFW	Transparent polycrystalline windows	351
-----------	---	-----

Vessel/In Vessel

Plasma Facing Components

UT-PFC&C-HIP	Mechanical behaviour of HIP joints	355
UT-VIV/PFC-BDG	Boron doped graphites	359
UT-VIV/PFC-SiC/MJ	Development of SiC/metal joining techniques	361
UT-VIV/PFC-W/Coat	Development of thick W CVD coatings for divertor high heat flux components	365
UT-VIV/PFC-TMM	Thermo-mechanical models	369

Remote Handling

UT-VIV/AM-Actuators	Remote handling techniques - Advanced technologies for high performances actuators	371
UT-VIV/AM-ECIr	Remote handling techniques - Radiation tolerance assessment of electronic components from specific industrial technologies for remote handling and process instrumentation	373
UT-VIV/AM-HMI	Remote handling techniques - Graphical programming for remote handling techniques	377
UT-VIV/AM-Hydro	Remote handling techniques - Technology and control for hydraulic manipulator	381

Tritium Breeding and Materials

Breeding Blanket

UT-TBM/BB-IMBLA	Improved breeding blanket	385
UT-TBM/MAT-LM/MAG	Liquid metal corrosion under magnetic field	391
UT-TBM/MAT-LM/Refrac	Compatibility of refractory materials with liquid alloys	395
UT-TBM/MAT-LM/SiC	Compatibility of SiC _f /SiC composites with liquid Pb-17Li	399
UT-TBM/MAT-LM/WET	Wetting of materials by liquid metals	405

Materials development

Structural materials

UT-TBM/MAT-BIM	Dissimilar diffusion-bonded joints mechanical testing	409
UT-SM&C-COR	Metal and oxide thermodynamic stability and solubility in water cooling systems	413
UT-SM&C-LAM/Weld	Laser weldability of LAM steels (Eurofer 97)	417
UT-TBM/MAT-LAM/Mic	Influence of the martensite morphology on the plasticity behaviour of the Eurofer steel	421
UT-TBM/MAT-LAM3	Microstructural investigation of Reduced Activation Ferritic-Martensitic (RAFM) steels by Small Angle Neutron Scattering (SANS)	425
UT-TBM/MAT-Mod	Modelling of the resistance of the dislocation network to the combined effect of irradiation and stress - Comparison of a pulsed and a continuous irradiation on the secondary defects structure in an annealed 316L steel	429
UT-TBM/MAT-ODS	Development of forming and joining technologies for ODS steels	433

Fuel cycle

UT-TBM/FC-SP	Separation of the D/T mixture from helium in fusion reactors using superpermeable membranes - Superpermeation : nonmonotonous energy dependence at low energy ion bombardment and the effect of membrane carbidization on hydrogen permeation through the niobium membrane	437
--------------	--	-----

Safety and Environment

UT-S&E-BLK	Blanket safety – Design of a test section for MHD experimental program	441
UT-S&E-Mitig	Evaluation and mitigation of the risk connected to air or water ingress	443

System studies

UT-SS-REL	Reliability / availability assessment - Double walled tube concept, impact on the pressure tubes reliability / availability	447
-----------	---	-----

<i>INERTIAL CONFINEMENT FUSION PROGRAMME</i>		451
ICF01	Intense laser and particle beams dynamics for I.C.F. applications	453
ICF02	Cryogenic targets production using magnetic levitation	457
ICF03	Laser-matter interaction at relativistic intensities and fast igniter studies	461
ICF04	European collaborative experiment on the fast igniter concept	463
ICF-KiT-PRC	Overview on power reactor concepts	465
<i>APPENDIX 1 : Directions contribution to the fusion programme</i>		469
<i>APPENDIX 2 : Allocations of tasks</i>		473
<i>APPENDIX 3 : Reports and publications</i>		479
<i>APPENDIX 4 : CEA tasks in alphabetical order</i>		491
<i>APPENDIX 5 : CEA sites</i>		497

Task Title : SUPPORT TO ITER DIAGNOSTIC DESIGN : POLARIMETRY

INTRODUCTION

The task objectives are to adapt the design of the polarimetry diagnostic to ITER FEAT design and to re-evaluate its performance in the revised plasma conditions, to provide support to the ITER JCT in the preparation of the relevant ITER documentation and in evaluation of the cost.

The contract is a collaboration between several European laboratories.

CEA takes part in some of the subtasks, which are:

- To re-evaluate the conceptual design of the polarimetry diagnostic for ITER FEAT.
- To propose concepts for the transmission line for the chosen frequency, to define the optical elements.
- To study the characteristics of the retro reflector which will be fixed inside the vessel.

2001 ACTIVITIES

In order to re-evaluate the design of the diagnostic, one has to evaluate how the infrared beams can be transported from the lasers to the plasma, then how they can be reflected to the detectors. In taking into account the localisation of the lasers and the inner mirrors, we have calculated the IR beam expansions and the necessary focusing mirrors. This allows dimensioning the mirrors and in particular the retro reflector corner cube (CC) that will be fixed inside the vessel. For a 118 microns wavelength, typical waist of 12 mm on the CC is compatible with a 37 mm diameter of the CC and leads to a 60 mm beam diameter on the first focusing mirror that is situated nine meters away. Then the beam is transported and focused by a second spherical mirror on the detector with a waist value of 1 mm.

Inside the plasma, the IR beam is refracted. Using a ray tracing code, we have calculated the effect of this refraction on the CC for a typical plasma scenario. The maximum expected shift on the CC is 6 mm and leads to recommend that the CC should be elongated in the vertical direction to support the refraction effect.

We also modified a beam ray tracing code to simulate reflection of the IR beam on the CC. This allows studying some spurious effects:

- The precision of the angles between the CC faces must be important; 0.015° of imprecision on each face leads to a total possible deviation of .1° of the output beam and a 33 mm shift on the first focusing mirror.

- When a CC is elongated, ray tracing show that the maximum of reflection is obtained when one of the interface is oriented parallel to the elongation.

One important point is to predict the effect of plasma irradiations on the CC optical properties.

We started the discussions to prepare numerical simulations of the phenomenon and to prepare comparative experiments of mirrors exposure to the Tore Supra plasmas in 2003.

The possible material of the CC is an alloy of Copper for the moment but others could be used like poly or mono-crystal Molybdenum or Tungsten.

We also started discussions on the calibration set of the diagnostic in order to be able to give recommendations on the usefulness of such a system.

In order to qualify the electronics, it was found that such a system has to be placed on the returning beam. It was also suggested that another should be installed before the CC to qualify the CC.

As the beam length path from the laser to the detectors are very long (more than 60 meters), discussion have been made on the different methods of alignment.

Both visible and IR methods were found to be useful and recommendations were made to prepare full-scale laboratory experiments.

Among the difficulties, the centring of the beam on the CC is critical because of the lack of access in the vacuum vessel and because the CC will not reflect the visible laser. Specific experimental tests need to be prepared with specific rotating mirrors and associated detectors.

CONCLUSIONS

Calculations have been made to dimension the mirrors, which transport the IR beam from the laser to the detectors, and also to define the inner corner cube mirror. No major difficulty has been found.

Preparation of experiments of characterisation of mirrors that will be exposed to plasma has been made. Tore Supra is proposed to be used as test bed during the next two years.

Discussions on the needed calibration system have been made and solutions were proposed.

Methods of alignment were discussed and recommendations on experimental tests, in particular to align the inner corner cube mirror, were elaborated.

REPORT

The final report is still in elaboration under the Euratom-FOM Association responsibility. It will contain the French contribution as well the ones from the other laboratories.

TASK LEADER

Christophe GIL

DSM/DRFC/SCCP
CEA Cadarache
13108 St Paul Lez Durance Cedex

Tél. : 33 4 42 25 49 26

Fax : 33 4 42 25 62 33

E-mail : gil@drfc.cad.cea.fr

Task Title : ITER DIAGNOSTIC WINDOW DEVELOPMENT

INTRODUCTION

The objective of the “ITER diagnostic windows development” was to develop, fabricate, and test a sapphire window-ferrule assembly, which will be located in the ITER cryopump port area. A window diameter of 20 mm has been selected in group-A.

Alternatively, polycrystalline ceramic windows of same size have been proposed by CEA.

The contract included also the modification and commissioning tests of the infrared irradiation test-facility (IRIFA) at DER-Cadarache. This installation allows, if required, testing of general window assemblies under heat loads at specified temperature gradients.

Whereas during the year 2000 the design of the ITER windows has been completed, manufacturing and testing has been performed during the first half of year 2001. Commissioning tests in IRIFA on a crystal quartz window started end of 2000. The fabricated ITER windows including the final report [1] have been delivered to the ITER -JCT end of august 2001 just in time.

2001 ACTIVITIES

SUMMARY OF ITER WINDOW DESIGN AND THERMO-MECHANICAL ANALYSIS

Thermo-mechanical stresses in window assemblies for different loading cases have been calculated for edge brazed sapphire windows (sapphire $\varnothing = 19$ mm) bonded to a nonmagnetic titanium- or copper-ferrule as well as for diffusion bonded titanium-ferrule design (Fig. 1).

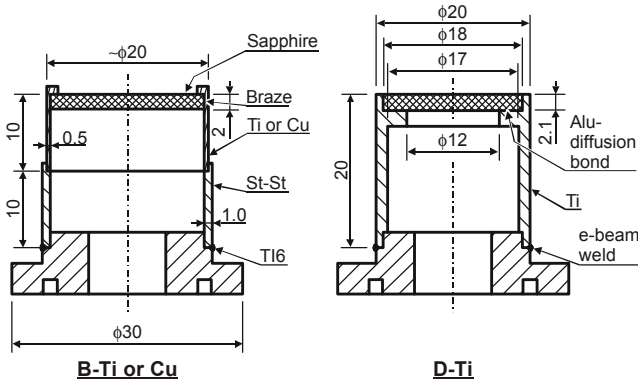


Figure 1 : Different investigated window assembly concepts for ITER cryopump port area

B-Ti or Cu : Edge brazed sapphire/titanium or copper OFHC ferrule bonded to a stainless steel body

D-Ti : Diffusion bonded sapphire/titanium ferrule design

Due to the difficulty of stress evaluation at the bonding joint area encountered in the TS endoscope head calculations [2], it has been assumed that the components are stress-free at R.T. and the bonding joint (braze or diffusion interlayer) has not been simulated. It should be mentioned that for the edge brazed window geometries and a required ferrule outer diameter of 20 mm, the window-viewing diameter is 19 mm (sapphire thickness 2 mm).

In the calculation a copper or titanium ferrule, which is bonded to a cylindrical stainless steel body, has been assumed. The industrial proposed diffusion bonded window design leads to a viewing diameter of only 12 mm by a same ferrule outer diameter of 20 mm.

A comparison of calculated maximum component and local (distance $\Delta \geq 0.5$ mm from singular points) sapphire tensile stresses and strains for such window ferrule designs is shown in Tab. 1.

Table 1 : Comparison of calculated maximum component and local* (distance $D \geq 0.5$ mm from singular points) sapphire window tensile stresses and strains for different ITER window ferrule assemblies

Loading conditions: P= 0.5 (MPa) T= 200 (°C)	Cu OFHC Ferrule l= 10 mm	Titanium Ferrule l= 10 mm	Titanium Ferrule l= 20 mm
Window Components	Edge brazed	Edge brazed	Diffusion bonded
Ferrule σ_{VM} max.(MPa)	69	212	110
Ferrule $\Delta\epsilon$ max. (%)	2.7	0.19	0.097
Body St-St σ_{VM} max.(MPa)	21	163	
Body St-St $\Delta\epsilon$ max. (%)	0.01	0.36	
Sapphire σ_{tt} max. (MPa)	58/-20	51/-21	94/-64
σ_{tt} loc. tensile*	15	15	65

For the edge brazed copper or titanium ferrule design the accidental pressure and baking case (0.5 MPa/ 200°C), which has been voluntary combined, leads to comparable stresses and strains in the sapphire windows, while the strain value in the titanium-ferrule is much lower. It should be mentioned that this type of ITER window is positioned far away from the radiation source and behind labyrinth viewing access lines, so that direct heat load effects are not a concern and neutron irradiation is reduced (total neutron flux about 0.7×10^{10} n/cm²s).

Similar sapphire window stress values (not listed in Tab. 1) are obtained for a simple titanium ferrule design without stainless steel body.

For the same loading case the diffusion bonded design shows higher local (distance $\Delta \geq 0.5$ mm from singular points) sapphire window tensile stresses ($\sigma_{tt} = 65$ MPa/cult.~200 MPa) than the edge-brazed assemblies (15 MPa).

Therefore an edge brazed overall nonmagnetic titanium-ferrule design has been preferred and a silver free (Au/Cu) window bonding procedure, if feasible, recommended in order to satisfy the ITER nuclear requirements (avoid Ag \rightarrow Cd transmutation under neutron irradiation).

WINDOW FABRICATION

The edge brazed window/ferrule assemblies are TIG welded to small test flanges of 30 mm diameter. First five sapphire window assemblies, which have been fabricated by *Saint-Gobain/Desmarquest* (France), leaked at R.T. (factory He test) after brazing.

According to the manufacturer, the brazing tool seems to have caused these failures. Consequently a new set of sapphire window assemblies has been fabricated according a classical Ag/Cu brazing procedure ($T \sim 800^\circ\text{C}$) in order to follow the safest fabrication route and to be in time with the ITER contract due time (Fig. 2).



Figure 2 : Manufactured sapphire/titanium ferrule assemblies and polycrystalline ceramic windows for ITER

As an alternative solution to sapphire, polycrystalline ceramic windows have been supplied by CEA Saclay [3]. The property of their cubic crystallographic system allows preparation of transparent material by using techniques of powder technology. Therefore Magnesium Spinel (MgAl_2O_4), which has an optical transmission as large as that of sapphire and an excellent swelling behaviour under neutron irradiation, as well as Yttrium Oxide (Y_2O_3) windows have been brazed to titanium ferrules ($\varnothing = 20$ mm) during the same fabrication batch.

ITER WINDOW TEST RESULTS

The ITER diagnostic window test specification for normal duty events and accumulated normal life before neutron irradiation foresees mainly:

He leak test (10^{-9} mbar.l/s) and visual inspection (during or after):

- Pressure differential (max. 0.5 MPa at R.T.) 3 cycles
- Temperature ramp (0-200°C) 10 cycles
- Vibration (15 g for 10 ms at R.T.) 1000 cycles

Pressure and temperature tests have been carried out in a vacuum facility. Transverse and axial vibration tests have been performed by *SOPEMEA/Velizy-France* using an electro-hydraulic shaker equipment (Fig. 3).



Figure 3 : Vibration tests on an ITER sapphire window assembly

All Ag/Cu brazed window types have sustained successfully the test requirements. However Yttrium Oxide windows seems to have become an aspect of reduced transparency after brazing, probably due to material desoxidation. Micro-porosities in the Magnesium Spinel windows have been observed already after sintering.

COMMISSIONING OF IRIFA

For commissioning of IRIFA [4] a crystal quartz window, which was available at Tore Supra, has been tested (screening) and should have been cycled under Tore Supra/CIEL requirements. It should be remembered, that the thermal radiation source in IRIFA is provided by an electrical resistor heater made of carbon-carbon fibre (CFC) composite material.

Therefore the loaded window surface has been covered with a temperature resistant thin film layer (painting) in order to absorb a substantial fraction ($\sim 90\%$) of the spectral emissive power of the resistor heater.

The window of 110 mm outer diameter and bonded via an aluminium-diffusion layer to a massif stainless steel body, has been provided by UKAEA.

For an “inside body” window incident heat flux of about 0.6 W/cm^2 during 1000 s, the window temperature attained 120°C ($T_{ini} = 25^\circ\text{C}$) with a centre to edge gradient of roughly 25°C . The body temperature varies between 36°C (upper part) and 90°C (bonding area).

The crystal quartz window failed (crack) during the first slow cool down cycle (Fig. 4).

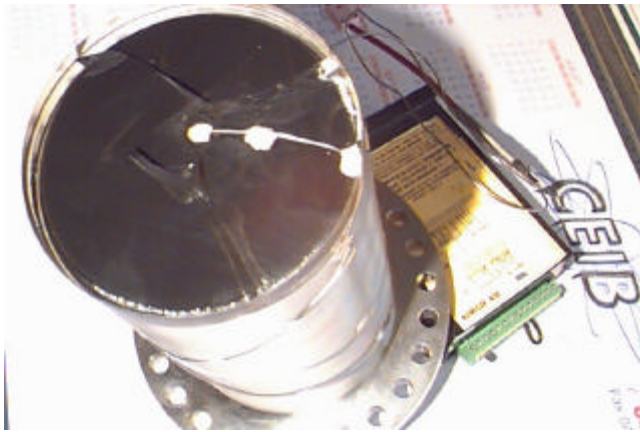


Figure 4 : Damaged crystalline quartz window assembly after commissioning tests in IRIFA.

Thermo-mechanical analysis (diffusion bonding joint not simulated, component assumed to be stress-free at R.T.) of the assembly show local (distance $\Delta \geq 0.5$ mm from singular points) tensile stresses of $\sigma_{tt}(\Theta) = 24$ MPa near the window bonding joint area compared to a crystal quartz ultimate tensile strength of $\sigma_{ult} \sim 88/110$ MPa. The disagreement between the heat flux test and the calculation results show, that the real component stresses (influence of bonding joint and material properties, associated creep effects and entire fabrication procedure) are finally unknown.

CONCLUSION

A non-magnetic edge brazed sapphire-window/titanium-ferrule assembly for ITER cryopump area has been developed and fabricated.

Although thermo-mechanical stress analyses of window/ferrule assemblies are difficult due to uncertainties in the simulation of the bonding joint area, the design concept has been selected following such a calculation procedure. Before neutron irradiation, all window assemblies have been tested successfully without damage. Due to fabrication difficulties during ITER window/ferrule assembling, an Ag/Cu brazing procedure instead of a recommended Au/Cu material has been used.

The modification of the infrared irradiation test facility (IRIFA) at DER-Cadarache has been performed and commissioning tests on a Tore Supra/CIEL crystal quartz window carried out. The disagreement between the heat flux test and the prediction of the associated thermo-mechanical stress analyses confirm, that appropriate qualification tests for window assemblies are needed.

REFERENCES

- [1] M. Lipa, Ch. Portafaix, "ITER diagnostic window development-task 5.1a(PE)", CEA/DRFC - Final Report, Cadarache, August 2001.
- [2] M. Lipa, Ch. Portafaix, E. Pluyette, N. Lochet et al., "Development and testing of diagnostic windows for Tore Supra/CIEL and ITER", ISFNT6, San Diego/USA, April 2002, to be presented.
- [3] F. Valin, "Transparent polycrystalline ceramic windows M.4.", Report-CEA/DTA/CEREM/CEM/LECMA D.T. 98/95 FV/FL, Saclay, 1998.
- [4] E. Pluyette, J.P. Dieppois, F. Challet et al., "IRIFA : Thermomechanical qualification of diagnostic windows under high IR radiative flux", ISFNT6, San Diego/USA, April 2002, to be presented.

TASK LEADER

Manfred LIPA

DSM/DRFC/SIPP
CEA Cadarache
13108 St Paul Lez Durance Cedex

Tél. : 33 4 42 25 46 58

Fax : 33 4 42 25 49 90

E-mail : lipa@drfc.cad.cea.fr

Task Title : SUPPORT TO ITER-FEAT LOWER HYBRID LAUNCHER AND TRANSMISSION LINE

INTRODUCTION

The goal of the study is to reassess the LH system for ITER - FEAT. Twenty MW LH is used in the steady state scenario in order to drive around 10 % of the total plasma current (9 MA) for pulse length larger than 400 s in the outer part of the plasma.

The LH system is composed of: a generator made of 24 one MW 5 GHz CW klystrons, a 60 meters long transmission line, one launcher.

2001 ACTIVITIES

FOR THE LAUNCHER

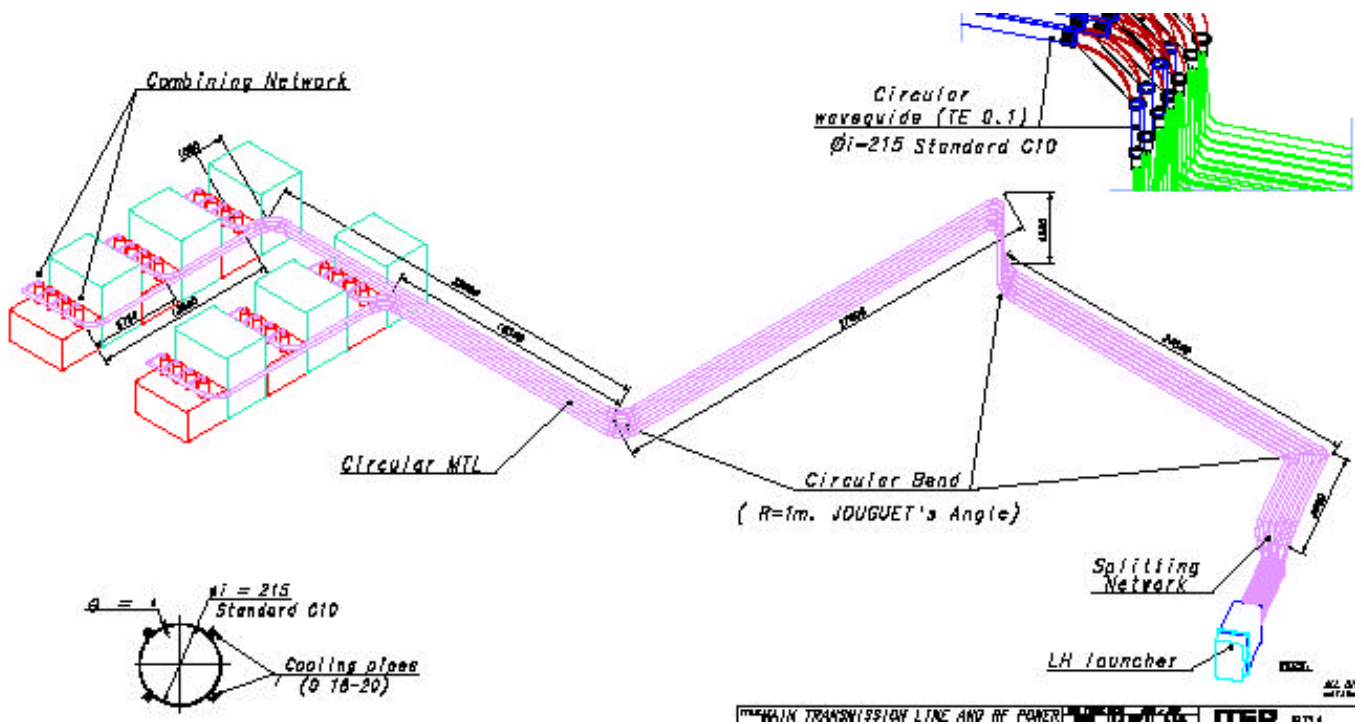
The drawings of the grill have been made taking into account the ITER FEAT environment and constraints.

The different following studies have been done:

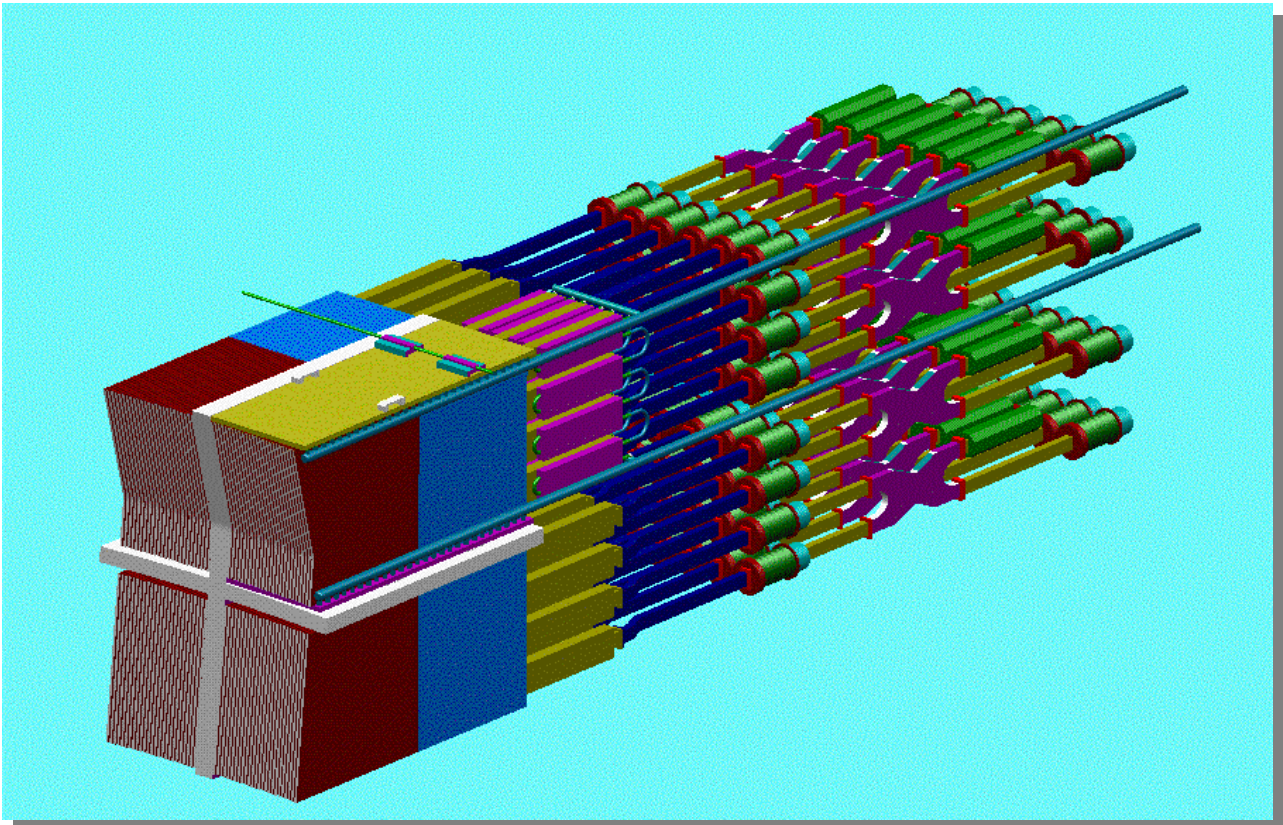
- after a brief description of the grill, a discussion is made on the chosen material and assembling techniques,

- the main RF components have been defined and computed, especially the mode converters and the tapers,
- the power density limit is given,
- a vacuum analysis is performed to compute the pressure inside the launcher for different degassing rate,
- the coupling properties are discussed,
- the mechanical stresses in the launcher during disruption are computed,
- thermal analysis are made which takes into account, plasma radiated power, RF losses, and neutron flux,
- the water cooling circuit is defined,
- the acceleration of electrons in the antenna near field is studied,
- neutron damping by the launcher is analysed.

The goal of the ITER task on LH is to study the design of the launcher and of the transmission line.



Overview of the ITER LH system

*LH Launcher*

FOR THE TRANSMISSION LINE

After a global overview of the transmission line, RF analysis have been performed for the different main components: splitting network, straight part, bend, mode filter, RF windows, Hybrid junctions, Water load.

CONCLUSIONS

FOR THE LAUNCHER

The design of the LH launcher has been adapted to the environment of ITER FEAT. It follows the general rules given for all the RF antennas. In the port of ITER FEAT, the radiating surface is sufficient to be able to inject 20 MW at a power density of 33 MW/m².

The antenna is modular and uses four identical blocks. Each block is a waveguide array of 12 x 24 active waveguides and 12 x 25 passive waveguides. The main components are hybrid junctions, mode converters and E plane 270 degrees multijunctions.

A first study of the different RF components of the antenna has been done. For some of them the definition is straightforward: hybrid junction, standard waveguides, bends, phase shifters, TE₁₀ taper.

Others will need more accurate studies and optimisation: multijunction parts, mode converter, TE₃₀ tapers, 3 waveguides H plane junction (at the output of the TE₃₀ tapers).

These computations must be then followed by the realisation of mock-up of the different element in order to check their RF capability.

The coupling properties of the antenna are good on a wide range of electron density. The concept of PAM (Passive Active Multijunction) allows to work near the electron cut-off density where the thermal loads are smaller.

For the choice of material, the main new thing is the use of beryllium to realise the passive waveguide. A mock-up made with the envisaged technology using dispersoide copper or CuCrZr and beryllium passive waveguides should be built and tested on a high power RF test bed.

The antenna can be efficiently water cooled in order to remove the power coming from the neutron damping, the RF losses and the radiated power from the plasma. A first drawing of the hydraulic circuit is given.

The launcher is sufficiently robust to withstand stresses due to Eddy current during disruptions. And the water-cooling is sufficient to control the amplitude of the thermal strains. The study has shown that Carbon Fibre Composite can not be used as a material for passive waveguides due to its too different thermal expansion. As a consequence beryllium is foreseen.

If the antenna is baked before performing shots on plasma, no added pumping seems to be necessary. And the pressure is small inside the launcher in any case.

The studies made on the acceleration of electrons in the antenna near field shows that the foreseen power flux is very small.

It is so small that it doesn't seem to be necessary to round the shape of the tip of the wall of the antenna. That means that if they are rounded, the margin is even larger.

The antenna is dense enough to damp the neutron in order that the activation is sufficiently low to be able to work hands on at the vacuum vessel flange.

The main difficulties still to be solved are:

- To find an efficient diagnostic in order to detect arcing at the plasma antenna interface. This in order to prevent to damage the mouth. An efficient way can be the use of $H\alpha$ spectroscopy. The measurement is proportional to the electron density.
- To allow coupling in every condition especially in H mode with elms. The antenna will be flush mounted and the distance to the separatrix is large. The distance to the electron cut-off density can be a few centimetres.

Two solutions are being studied :

- * gas injection near the launcher,
- * use of other ECRH or LH with waveguides specially devoted for that purpose. There is place in the outer part of the ITER FEAT LH antenna where waveguides could be easily inserted.

In order to check the proposed LH design, it would be really interesting to have test performed with ITER FEAT like design.

The PAM concept will be tested on FTU in order to control its coupling capability and its power handling capability.

It would be then safe before to realise an ITER FEAT one scale antenna to built an ITER like antenna which can be tested on Tore Supra due to its long pulse capability and or in JET to study the coupling in conditions which are relevant for ITER.

FOR THE TRANSMISSION LINE

The transmission line of the LH system of ITER FEAT has been described and analysed. The main originality in the design is the use of a main transmission line made of 6 circular oversized waveguides that link the 24 klystrons to the antenna. Each circular waveguide is fed by 4 klystrons with a combining structure at the input and is then split at the output into 4.

To protect the oversized transmission line from reflected power that could excite spurious mode and also to divide the power into 2, hybrid junctions are used in the transmission line situated in the cryostat.

Many components used in the design are "standard" ones WR229 rectangular waveguide, RF windows, High power loads, Hybrid junction.

The next step for these components is to realise a prototype that can be checked at high power.

Other components are less standard. They need more evaluation.

From the theoretical point of view, the results of the first studies are promising. But more accurate analysis is necessary.

For the splitting network:

- the transition from rectangular to sector has to be optimised,
- the accuracy which is needed in the realisation of the component must be evaluated,
- the analysis of reflected power coming from the antenna must be assessed. What is the dependence with the relative amplitude and phase of the backward waves ?
- the analysis of the effect of losing one klystron must be done.

This last point can be detrimental. This would mean that when a problem is encountered with one klystron, this leads to the loss of 4 MW. In this case the only solution is to come back to a design with 24 independent transmission lines. But it is another study.

For the bends, more accurate studies must be done using finite element code.

For the mode filters more accurate analysis are needed.

For the straight circular waveguide, no diffraction losses have been considered. A study of the effect of misalignment, shape defect on the excitation of spurious modes must be done.

After these studies, mock-up have to be done with associated technique of measurement using electric field determination by probes or determination of radiated pattern.

These steps being crossed with success, components must be done for the test at full power.

REPORTS AND PUBLICATION

Report on ITER-FEAT launcher, Contract FU05 - CT 2001-00019 (CEA : EFDA/00-553, ENEA : EFDA/00-554)

Report on the transmission line of the LH system on ITER FEAT, Contract FU05 - CT 2001-00019 (CEA : EFDA/00-553, ENEA : EFDA/00-554)

TASK LEADER

Ph. BIBET

DSM/DRFC/SCCP
CEA Cadarache
13108 St Paul Lez Durance Cedex

Tél. : 33 4 42 25 49 87
Fax : 33 4 42 25 62 33

E-mail : pbibet@cea.fr

Task Title : SUPPORT TO ITER ICRF SYSTEM PHYSICS AND ENGINEERING DESIGN

Electrical design of an ICRF array for high RF power density in ITER-FEAT

INTRODUCTION

ITER-FEAT operation will be now largely driven by auxiliary heating and current drive systems. The reduced port dimensions and the increased competition for plasma access among subsystems has led to increased heating power density requirements. For the Ion Cyclotron System, the design target of 20 MW/port (i.e. a power density of ~ 9.3 MW/m²) represents a roughly twofold increase compared with the ITER-FDR design. It would mean operating at RF electric fields higher than those routinely obtained in most of present-day experiments, with associated unknowns about E-field driven RF sheaths losses, and voltage standoff limitations.

Besides, ICRF coupling reliability is essential to drive ITER-FEAT scenarios, in particular to guarantee H-mode operation, in spite of fast transient load variations (ELMs, MHD).

Hence, changes in the layout of the IC array has been recognized to be necessary to:

- i) reduce the operating voltage (in particular at the plasma/array interface) with target values of electric field module below 2 kV/mm for E parallel to B, and 4 kV/mm for E perpendicular to B.
- ii) increase its tolerance to load variations with a target VSWR value < 2 to be maintained at the (tuned) array input for variation of the coupling resistance from 2 to 10 ohm/m

2001 ACTIVITIES

Different design options and layout modifications to the original Resonant Double Loop (RDL) concept were studied. The IC launcher designed in ITER-FDR consisted in an array of 4 toroidally x 2 poloidally standard stripline Resonant Double Loop (RDL) antennas.

In the several configurations studied, the number of rows of the launcher array has been kept unchanged to 4. Increasing the number of rows has not been considered not only because minimum space requirements but also because for two-conductor striplines, reducing the strap width would lower the coupling resistance.

Consequently for a given maximum voltage (or electric field), the power which would be possible to launch from a row would be reduced, leading in the end to a predicted unfavourable trade-off.

In the poloidal direction, the array is taken to be top bottom symmetrical.

For the comparison between options, one cell of the array has been considered, which accounts for one eighth of the array total surface.

Two main studies, including geometrical layout description, matching analysis, and RF voltage/current distribution calculations have been conducted:

1. Segmented antenna option

A segmented antenna configuration (cf. fig. 1) was first studied.

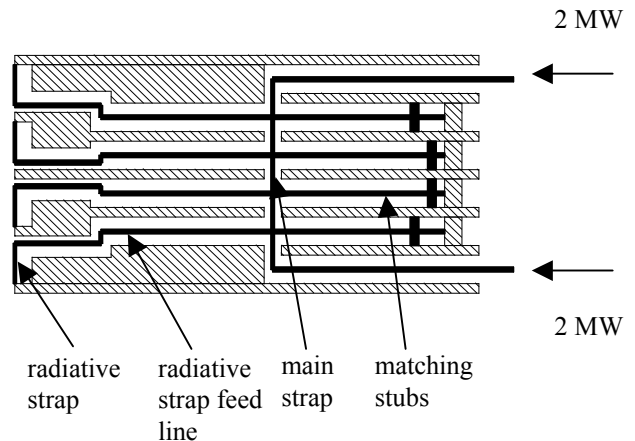


Figure 1 : Segmented antenna layout

Sharing of the power (and consequently of the electric field) among the different radiative straps is the main issue that was identified on this option. In the case of same RF electrical properties for the 4 single straps, the power distribution is very unequal due to RF voltage / current resonant distribution in the main strap (up to 95 % of the power actually goes in the inner straps). As the power brought to each radiative strap is proportional to:

- the square of the voltage amplitude on its feed line to main strap connection and to,
- the real part of the admittance at the same point.

we could think of playing with the radiative strap feedline lengths in order to flatten the voltage distribution on the main strap and try to balance the power distribution, but this happen to lead to severe limitations on the antenna operative frequency range.

Given the conceptual issue coming out of this study of the segmented configuration, and the port size issue for the RDL configuration, the design has moved to “non standard” RDL configurations

2. “Non standard” RDL option

The “non standard” RDL configuration sketched in fig. 2b) was then studied.

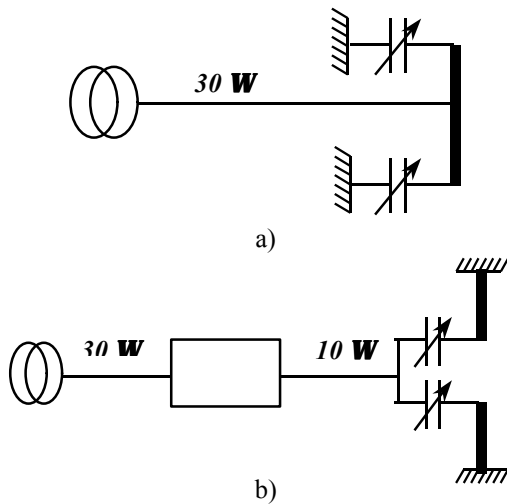


Figure 2 :
 a) Standard RDL layout (Tore Supra experiment)
 b) “Non standard” RDL layout

The new RDL configuration happens to have two main advantages against standard type:

- A better mechanical holding of the straps, which is much profitable to withstand disruption loads.
- Nice electrical load -tolerant properties.

A sketch of a possible physical implementation of this configuration is given in figure 3, where the matching capacitor are made by an adjustable stub, put in series to the strap feeder through a coaxial quarterwavelength choke.

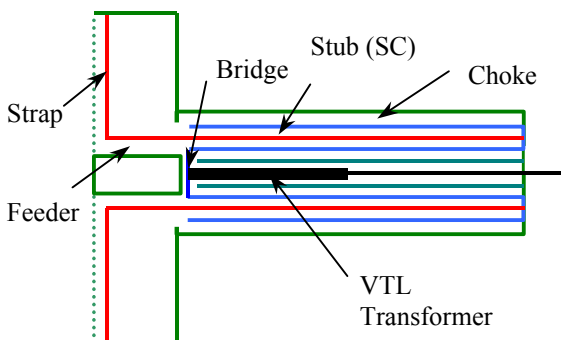


Figure 3 : Possible FEAT physical implementation

The nice load-tolerant properties (see in fig. 4 a typical comparison with standard RDL) is explained through an analytical derivation of the top/bottom symmetrical RF configuration. The key parameter is the ratio R_m / R_0 where R_m is the real part of the impedance at feeder end for the reference plasma loading target and R_0 is the feed line characteristic impedance.

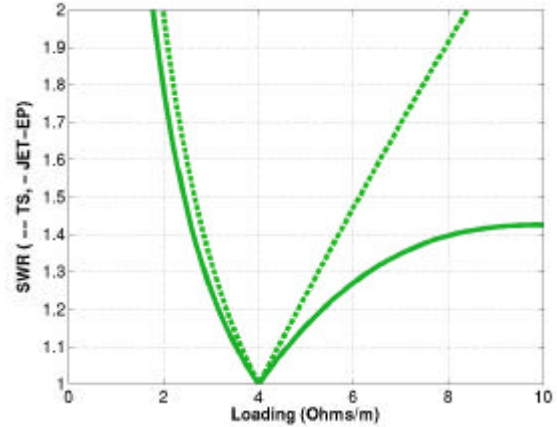


Figure 4 : Typical load tolerance properties (Standing Wave Ratio versus plasma loading for standard RDL : and “non standard” RDL)

Matching algorithms, and foreseen voltage and current distribution were calculated on the 40-60 MHz band. Three main points are to be reminded:

- Care should be taken in the detailed design to be sure that the feeder length is not too long as regards the matching condition, which may be simply expressed in the symmetrical case as: $R_m < 2 R_0$.
- The bridge section could bring some unbalance between the two strap currents and voltages (current and voltage amplitude of two identical straps become equal if the bridge length is set to zero). The effect of the bridge is clearly seen as detrimental in terms of power handling due to higher voltage maximum, and maybe in terms of poloï dal spectrum due to curent unbalance. More accurate modelling including non-TEM modes effect and/or mock-up measurements are desirable to get a better view of the “bridge effect”.
- The physical implementation based on low impedance (because of limited volume available) adjustable stub and choke exhibits quite high RF current at shorts and significant RF electric field at the stub mouth. Care should be taken on this issues in the detailed design, along with study of possible use of compact capacitors.

CONCLUSIONS

The motivation of the study, as detailed in the Task specification, was to investigate Ion Cyclotron Array design options for high power density operation, namely in the range of 10 MW/m^2 , a next step target which is significantly

higher than what is routinely achieved in present day experiments.

Let's recall the conceptual background of the above study: As voltage standoff at the front end of IC Arrays is commonly regarded as the main power limiting factor, the basic idea is to look for an electrical configuration with a low value of the RF electric field at the plasma interface. As IC antennas radiating straps are to be included in resonant circuits in order to match plasma load to transmission line impedances, low value of RF electric field can be obtained in the vicinity of physical or virtual grounds, with as practical consequence the need to use short straps. Short straps around physical or virtual grounds are all the more attractive as RF current are maximum around them, which, for a given coupling resistance, maximises the power capability.

The analysis performed both on the segmented antenna concept and on the "non standard" RDL concept brings a common conclusion: the main design issue towards IC high power density Arrays is the sharing of the power between straps.

The segmented antenna concept in its present layout is not satisfactory as far as the above issue is concerned. Some modifications might be included which nevertheless seem at this point difficult to match the frequency bandwidth requirement, which are close to an octave.

The RDL concept has the advantage to produce an intrinsic quite nice sharing of the power in its standard shape. The non standard option present in addition very nice load tolerant properties which allows to solve not far from completely an other important issue of IC antenna electrical design, namely ELM resilience. Some detailed design issues have been pointed out, which will require more accurate design optimisation with the aid of 3 D EM code and mock-ups validations. Finally, further R&D work is seen desirable on the matching components: ITER-FEAT relevant compact capacitor solutions and sliding contacts developments are to be pursued.

REFERENCES

- [1] G. BOSIA et al., High Power density Ion Cyclotron Antennas for Next Step Applications, 19th IEEE/NPSS Symposium on Fusion Engineering - Atlantic City (New Jersey) (USA), 22/01/02 - 25/01/02

REPORTS AND PUBLICATIONS

- [1] S. Brémond, EFDA Contract 00/546 Final Report, Electrical design of an IC array for high RF power density in ITER-FEAT, CEA Report DSM/DRFC/CH/NTT - 2001.015, September 2001.

TASK LEADER

Sylvain BRÉMOND

DSM/DRFC
CEA Cadarache
13108 St Paul Lez Durance Cedex

Tél. : 33 4 42 25 76 41

Fax : 33 4 42 25 62 33

E-mail : sbremond@cea.fr

Task Title : DEVELOPMENT OF VACUUM COAXIAL CAPACITORS FOR THE ITER-LIKE ICRF JET ANTENNA

INTRODUCTION

This contract was signed at the end of November 2000 in order to investigate the feasibility and the reliability of RF capacitors derived from commercial types for a special application to the JET antenna. The contract covers the purchase of 3 capacitors, the use of a high power test stand for the assessment of the failure rate, and the manpower resources to follow the fabrication and perform the relevant tests.

2001 ACTIVITIES

The capacitors have been ordered to COMET (Bern, CH) according to the specifications of the contract EFDA 00/569 : the order was sent on the 13th of December, 2000. The fabrication, initially foreseen for a duration of 30 weeks, took in reality 38 weeks since they were delivered to Cadarache on the 7th of September, 2001 (Fig.1). They are numbered #J7432, #J7434 and #J7435. The preliminary acceptance AC tests were performed on the 26th of September, and the RF tests took place between the 11th of October and the 4th of December.

The specifications were agreed as follows (table 1):

Table 1 : Design Parameters of the Prototype Vacuum Capacitors

No. of Capacitors	3
Frequency range (MHz)	30-60
Capacitance range (pF)	40-400
Operating temperature range (°C)	40-60
Operating pressure of cooling system (bar)	3 bar (abs)
Maximum peak RF voltage over the whole bandwidth (kV)	33
Maximum peak RF current over the whole bandwidth (kA)	1.3
Maximum pulse length (sec)	20
Maximum duty cycle	0.03
Number of axial full-stroke cycles	5,000
Tan δ	~ 10-3
Maximum stray inductance (nH)	< 60 nH
Mechanical dimensions	As per COMET CV3W-500F

Finally, the COMET capacitor retained is the CV3W 50-400 DB.

It is derived from a commercial type, but includes several special features :

- A stainless steel internal bellows, which is copper plated.
- An outer second bellows, which allows to adjust the capacitor by a push/pull action, and avoid any seal (DB = Double Bellows).
- Thicker outermost electrodes to cope with a high current (920 Arms or 1300 Apeak) for 20s.
- 2 corona rings to protect the ceramic edge.

Fatigue tests have been performed on test samples in conditions relevant to operational constraints. The conclusion from the manufacturer is that the test result, 11.500 and 11.504 full cycles, shows a very small dispersion. Hence the recommended number of 5.000 cycles can be guaranteed with a safety factor of more than 2.

The protocol has been agreed between EFDA and CEA. 2 types of tests are detailed : AC acceptance test and RF tests.

Acceptance tests have been performed on a special equipment featuring a 100 kV AC source in series with a current limiting resistor. It is equipped with an arc counter to monitor the number of arcs. The results of the acceptance test are : the 3 capacitors have passed the test on the 26th of September without any arc at any stage. They are accepted for further RF tests.

The RF test bed consist of a twin stub tuners system, and a 9" 30 W pressurized transmission line. It is powered by one of the TORE SUPRA high power generator.

The length of the different sections of transmission lines has been modified to be able to obtain impedance matching at the generator side of the tuner system at both ends of capacitor range. The following sketch (figure 1) shows the test stand configuration.

A resonant circuit is composed of the capacitor under test, the sections L4, L3, L2, and the stub S1, suitably adjusted for matching. The maximum voltage in this section is measured by the directional coupler.

The Stub S1 is a 3m motor driven stub which had to be modified for improved cooling. An external PVC tubing and a fan blower has been fitted on this stub to allow the repetitive RF pulses foreseen for the capacitors qualification.

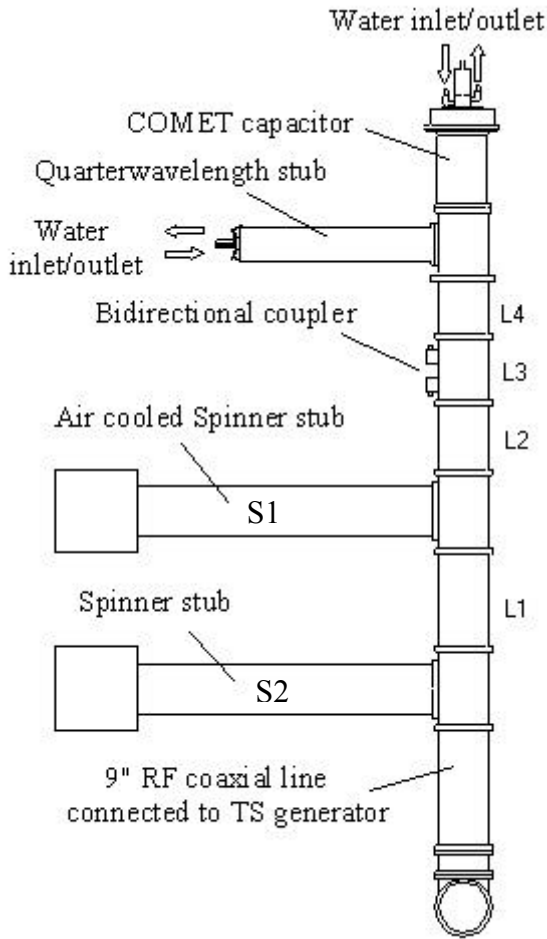


Figure 1 : Test line lay out

From the length of the different sections, the value of the maximum and minimum capacitance, and the self inductance of the capacitor, the ratio of the current (resp. voltage) in the capacitor to the maximum current (resp. voltage) in the line can be calculated.

The following figure (figure 2) shows how the capacitor is fitted at the end of the line.

It is held on the variable end by a thin flexible copper diaphragm.

On the fixed end, it is bolted to the coaxial inner conductor.

An external bracket, not shown here, keeps the capacitor in place when the line interspace is pressurised with 3 bar of dry nitrogen to increase the voltage standoff.

The 3 capacitors have been tested et voltage and current maximum.

The following traces (figure 3) show an example of the current in the capacitor, and the forward and reflected power on the generator output.

On the thermal aspect, the cooling circuit allows to make a rough estimate of the power dissipated on the variable end of the capacitor.

Hence, in the 20 s pulse shown above, the cooling flow is 389 g/s, and the temperature difference between input and output is roughly 3.8°C (see figure 4).

The power extracted by this circuit corresponds to about 6 kW, both from direct calculation at $t = 20$ s or from the integrated $\Sigma \Delta t * dt$ on this plot, in agreement with the theoretical values.

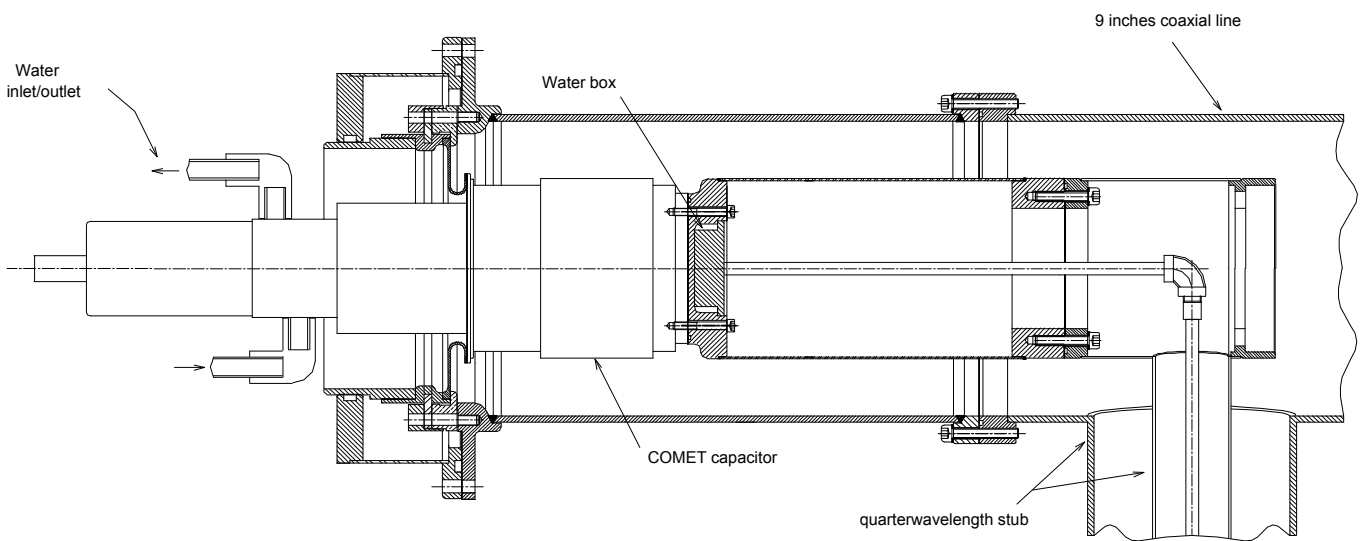


Figure 2 : Test device for JET-EP coaxial capacitor (60 MHz, 1000 Amps RMS, max pulse length 20s)

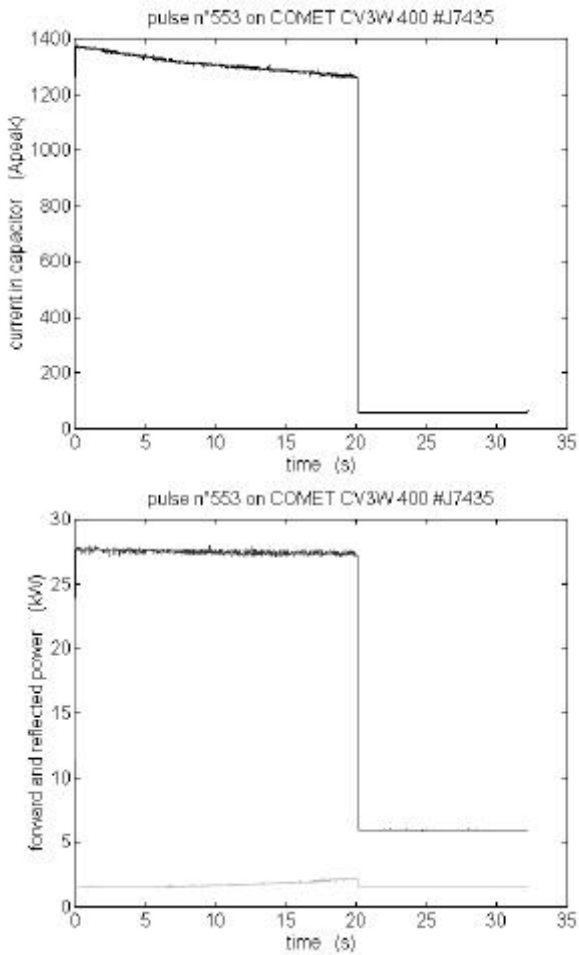


Figure 3 : Example of 20s pulse at 1300 Apeak level

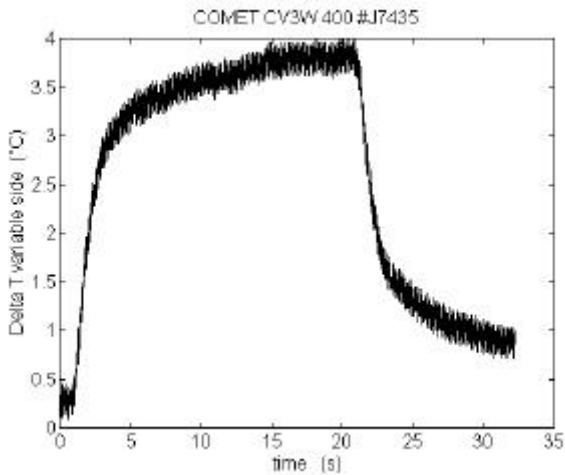


Figure 4 : Variable end cooling : temperature increase during a 20s pulse

CONCLUSIONS

Fatigue tests on bellows and guiding system sub assembly has shown that there is a good margin as regards the fatigue limit. In addition, no capacitor has ever had a fatigue failure in more than 10 years of use on Tore Supra, where each capacitor is in operation for a period of 3 to 4 years.

Failures on Tore Supra were related to corrosion through the bellows, which was made of Cu-Be, and is now replaced in these new units by a stainless steel component.

The 3 capacitors have successfully passed the RF tests at the current and voltage levels required in the contract. No limitations have ever been found in the range of parameters used during tests :

- voltage or current maximum : 33kVpeak or 920 Arms,
- RF pulse duration up to 20 s,
- repetitive RF pulses (in excess of 5000 for one capacitor),
- the self inductance measured by COMET is 15 nH.

The voltage limit of the capacitors are above 42 kV, but could not be more precisely studied since the test stand itself is arcing first. A 42 kV level correspond to +27% above the specifications, that is to say +60 % in power, but one must keep in mind that depending on the frequency, the limit in the antenna can be found on the current (pulse length limit) or on the voltage (power limit).

A few arcs have been observed in the test stand itself, which was operating close to its limits. A temperature monitoring of different points on the test stand showed modest variation (the most important one being the thin copper sleeve used to provide flexibility in the mechanical assembly).

REFERENCES

- CH/NTT-2001.003 : "Final Report on JET-EP /ICRH Antenna Design activities EFDA CSU No JW0-OEP-CEA-03".

REPORTS AND PUBLICATIONS

- CH/NTT-2002.001 : EFDA 00/569 contract : Final report " Vacuum Coaxial Capacitors for JET-EP ICRF Antenna ".

TASK LEADER

Bertrand BEAUMONT

DSM/DRFC/SCCP
CEA Cadarache
13108 St Paul Lez Durance Cedex

Tél. : 33 4 42 25 61 32
Fax : 33 4 42 25 62 33

E-mail : b.beaumont@cea.fr

Task Title : ICRF ANTENNA AND VACUUM TRANSMISSION LINE DEVELOPMENT

ICRH Antenna coupling : near field computations part II

INTRODUCTION

In previous ICRH antenna coupling studies [1] only the near field computations vacuum and the ITER antenna modelling have been made.

The objective of this activity was to compute the near fields in front of the ITER with realistic plasma parameters and to estimate the amplitude of the different components of the electric field. However we have also study the dependencies of the angle between the magnetic field line and the screen blades, look at the role of the metallic plate surrounding the ITER antenna and justify our assumptions.

The aim of this study is to know if the electric field amplitude is low enough to avoid some spurious effects as arcing or hot spots and to provide data to compute the RF sheath in front of the ITER antenna.

2001 ACTIVITIES

The report is organized as follows: at first the accuracy and the convergence conditions are given for the ITER antenna computations. In the following section, the plasma parameters and the operation conditions are specified and commented. After that, the choices used to describe the ITER antenna are justified and the eventual consequences and limitations are discussed. In the last section, the near field computations are presented in the monopole and dipole configurations.

CONVERGENCE TESTS AND ACCURACY

The theoretical description of the ICANT code can be found in the reference [2].

For the numerical calculation, equation (1) of [2] has to be truncated in the (k_y, k_z) space and only a finite number of modes (m, n) are taken. Hence calculated quantities reach their asymptotic value only if the limits of m and n are high enough. These limits depend on various parameters, such as the excited wave number k_0 and the minor and major radii a and R , but above all on the size of the smallest antenna element used in the antenna description. Good accuracy is generally obtained with a number of modes given by the inequalities $n > 3\pi R/\Delta w_z$ and $m > 3\pi a/\Delta w_y$ where Δw_z and Δw_y are the smallest dimensions of the antenna elements.

However, lower limits (by a factor of 2 to 3) can be chosen if one wants only the current profile or the real part of the power, whereas the convergence is weaker for the imaginary part of the power.

The calculation of the electromagnetic field near the antenna needs generally more modes, because smaller antenna elements are required to accurately describe steep field gradients that can occur locally (roughly speaking the shortest gradient lengths that can be resolved are of the order of half the element size).

For example, with the above criterion, for a single strap in vacuum [2], the electric field structure varies by less than 1 % once more than 10 current elements are used to model the strap.

As we use a Galerkin method, it is expected that the condition that the tangential electric field vanishes on conductors is satisfied on the average, and the maximal residual value of the tangential electric field decreases with the number of elements.

For instance, with a strap antenna and its finite Faraday screen, for 10 current elements on the strap and 7 current elements on each screen blade the maximal residual value of E_z on the strap, normalized to the value of E_z in the screen plane between the blades, is 2.5 %. For 15 elements on the strap it decreases to 1 %.

On the other hand the maximal number of elements is bounded due to the memory size of the computer and the computation time.

Note also that the computation time increases much more rapidly than the number of elements, because taking more elements means also taking more modes.

Finally, for the calculation of the 16-strap ITER antenna, at a frequency of 55 MHz, with $a = 2$ m and $R = 6.2$ m and an element size of 6 cm (2400 current elements), a spatial resolution of 2 cm for the fields requires 600 k_y -modes and 2000 k_z -modes.

The accuracy remains acceptable with 7 current elements on each strap, the error tangential electric field on the strap (normalized as above) being less than 5 %.

For this last case the main limit comes from the available memory size, 1 Go, and the computation time is 14 days on a DEC-Alpha workstation with a 666 MHz processor.

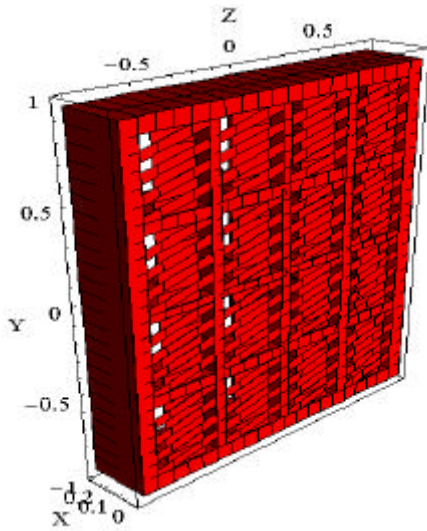


Figure 1 : ITER Antenna modelling with $\alpha = 16^\circ$ (coordinates in metres)

PLASMA PARAMETERS AND OPERATION CONDITIONS

The ITER-FEAT plasma parameters are used to compute the electric field (magnetic field $B_0 = 5.3$ T, plasma density at the centre $n_{\text{centre}} = 1$ or $1.5 \cdot 10^{20} \text{ m}^{-3}$ and frequency $\nu = 55$ MHz). After that, we show different cases where the plasma is modelled by a step function or a more realistic density profile ($n_e(r) = n_{\text{centre}}(1-(r/a)^\alpha)^\beta$ in the core where $\alpha = 2$ and $\beta = 1/2$ or 1), exponential in the SOL and a step at the edge with a typical value $n_{\text{edge}} \approx 10^{18} \text{ m}^{-3}$ (see Fig. 2).

The phasing corresponds to a monopole or a dipole with different angles for the screen blades. The geometrical ITER antenna characteristics are given in [1]. The unspecified coordinates on figures are expressed in meters.

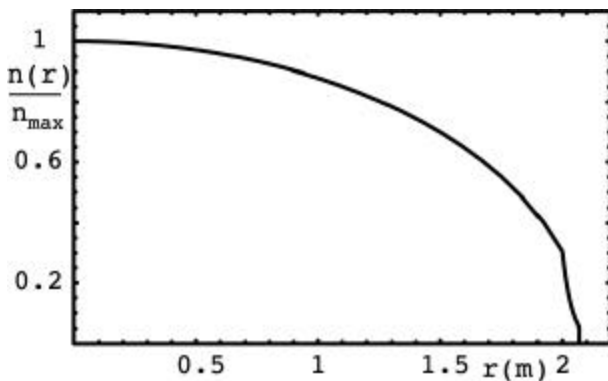


Figure 2 : Normalised density profile ($\alpha = 2$ and $\beta = 1/2$)

But some parameters stay undefined as the exact position of the last closed surface (LCS) and the shape of the density profile in a standard regime (λ_{SOL} characteristic length of the scrape-off layer (SOL)).

The λ_{SOL} value has been computed depending of the chosen density value at the edge for a given value of the density at the LCS. The range of λ_{SOL} values is 0.02-0.06 m.

The heating scenario considered here is a minority heating in the case of the fast wave (FW). In the case of inhomogeneous plasma including a temperature profile, the FW impedance matrix is computed with BRAFFA code [2]. The BRAFFA code can take into account the fraction of the minority species in % (Hydrogen or Helium ~ 1 %). The role of the slow wave can be ignored due to the finite Faraday screen [3].

CHOICE JUSTIFICATIONS AND LIMITATIONS

Several assumptions have been made during the ITER antenna modelling taking into account the main effects on each part of the antenna and some rules have been defined [1] and partially justified during the convergence tests. Here we justify some physical approximations.

We have considered that the slow wave remains a correction to the near field because there is a Faraday screen and also because the density in front of the screen is higher than 10^{18} m^{-3} . But without faraday screen the effect of the slow wave cannot be neglected. Indeed, for an unscreened strap, especially at low density ($n_e < 10^{18} \text{ m}^{-3}$), the effects induced by the slow wave on the radiated power become more and more significant as the launched frequency increases. As the frequency is increased the density at which the lower hybrid resonance is taking place also increases, moving the antenna coupling peaks associated to the slow wave to higher density. On the contrary, because the wavelength becomes shorter at higher frequency, the main peak corresponding to optimal density shifts to lower density, such that they ultimately merge (around 100 MHz).

For the inhomogeneous plasma, the antenna coupling variations are of the order 30 % between $\beta=1/2$ and $\beta=1$ for a given edge position. The coupling becomes lower when the density gradient increases. A density higher than the optimal density [2] can explain this. When plasma step model is used, we use a smaller value of the density to have a similar coupling level.

Magnetic shielding has been studied on the different parts on the antenna structure. The magnetic shielding effects on the thin strap can be neglected in spite of the transverse profile modification of the density current [2]. The effects of a thick strap are still an open question. The figure 3. shows that the radiated power (for a given peak current on the ground element) increases linearly with the thickness.

The current distribution shows that the y-component of the current on the screen front flows in the same direction than the current on the strap and is closer to the plasma, hence it efficiently contributes to the power. One can note, however, that magnetic shielding effects at first cause a decrease of the radiated power compared to the infinitely thin screen case (asterisk on figure 2).

This adverse effect was already discussed by Faulconer [4]. Similarly the propagation constant β on the strap starts from a lower value than for the thin screen value (1.09 instead of 1.096) and increases slightly with the bar thickness.

The antenna spectrum is also modified [3], although it is difficult to infer the effect on the coupling. Of course, the modelling of thick conductors significantly increases the number of elements in the computation. As the thickness of the screen blades is in the vicinity of the value where the radiated power is equal to the radiated power of a thin strap, the strap of the ITER antenna can be considered as thin.

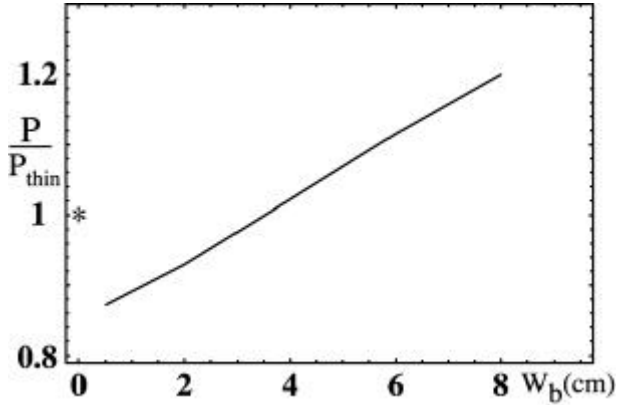


Figure 3 : Normalised radiated power versus thickness of the screen blades

Surrounding metallic wall effect on near field: The modelling of the ITER antenna restricts the wall only to the box around the strap but some high values of the electric field are around the corners of the box.

These values decrease when you put lateral protections. As the ITER antenna project shows that the faraday screen is surround with a metallic plane. Under these conditions we have to check the role played by this metallic plane and we have shown that the electric field is reduced near the corner of the antenna box (fig. 4).

This reduction is associated to a spreading out of the current on the metallic surface.

For the ITER antenna, the amplitude humps of the electric field at the corners of the antenna modelling should be reduced numerical or the antenna modelling includes a metallic wall. But the last proposition seems to be difficult to include due to the computer limitations.

The other parts of the antenna should include the magnetic shielding as the septa, the antenna box, the lateral protections.

CURRENT DISTRIBUTION AND NEAR FIELD COMPUTATIONS

The near field computations are associated to current distributions are made with the ITER plasma parameters given previously in different cases of the antenna structure (tilted or not screen blades), phasing (dipole 0,δ,0,δ or monopole 0,0,0,0) and plasma models (step, inhomogeneous with $\alpha = 2$, $\beta = 2$, 1 or 1/2).

The discrepancies in the current distribution between plasma step and inhomogeneous plasma models appear on the box and the asymmetries are located near the corner in the case of the inhomogeneous plasma. The variations of the near field follow the differences between the computed current profiles but those stay small.

The propagation constants change also in the same as the radiated power. Notice that the currents on the septa and on the box are multiplied by a factor 4 to have easy look at the current distribution.

It has been shown numerical that the main role of the septa is to reduce the parallel component of the electric field. However the z-component is significant at the edge of the box and can create asymmetric RF sheaths at the corners of the antenna. As expected, the current distribution on the antenna structure is highly modified between dipole and monopole configurations (see fig. 5).

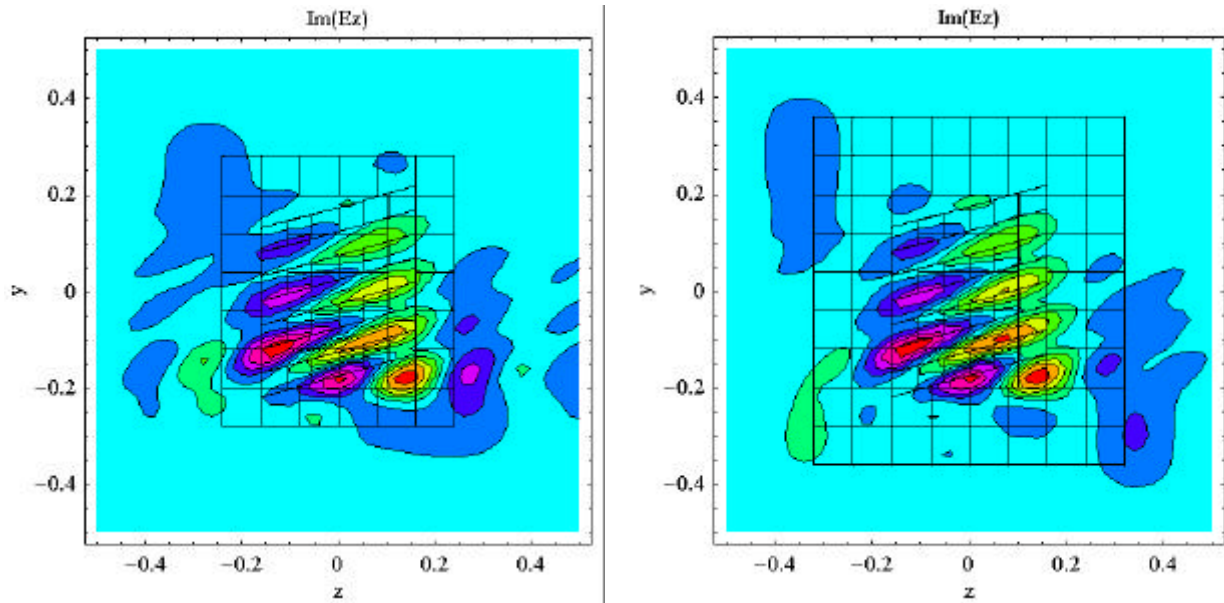


Figure 4 : The E_z component of the electric field without and with additional metallic plates

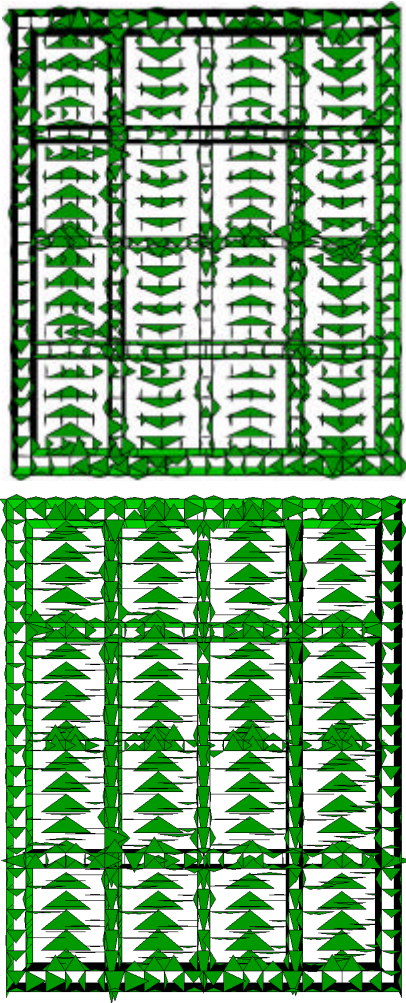


Figure 5 : The current distribution on ITER antenna structure in dipole (up) and monopole (bottom) configurations with inhomogeneous plasma with tilted screen blades ($\alpha = 16^\circ$)

In the monopole phasing, the septa bear higher induced current than in the dipole case. But locally the current can be higher on the box in the dipole configuration. These results are obtained without a metallic plane around the box.

In the case of a misalignment between the screen blades and the magnetic field line, the variations on the near field stay small if we consider the amplitude of the z-component of the electric field. But the structure of the near field follows the screen blade orientation. This situation can induce significant variations on the RF rectified potential [5] mainly due to the modifications of the path along a magnetic field line through the near field.

The coupling is low because the LCS is at 10 cm from the screen and the density at the edge (4 cm from the screen) is low $n_{\text{edge}} = 5 \cdot 10^{17} \text{ m}^{-3}$. For a radiated power of 20 MW in the case of monopole configuration with inhomogeneous plasma with tilted screen blades ($\alpha = 16^\circ$), the maximal value for the E_y component of the electric field is $\approx 7.5 \cdot 10^4 \text{ V/m}$, for $E_x \approx 2 \cdot 10^5 \text{ V/m}$ and for $E_z \approx 3 \cdot 10^4 \text{ V/m}$. If we reach the expected value of antenna coupling, these values can decrease by an order of magnitude.

The comparison with the plasma step goes to the same conclusion as before.

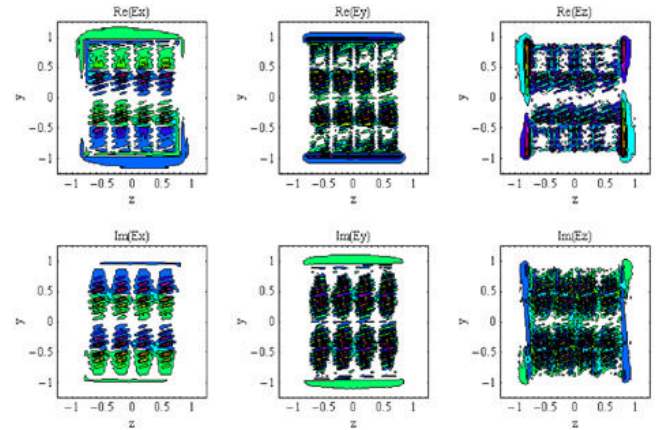


Figure 6 : Contour plots of the re normalised electric field components for an inhomogeneous plasmas at $r = 3 \text{ cm}$ with monopole antenna ($\alpha = 16^\circ$, grid 101×101 with $D_y = D_z = 2.5 \text{ cm}$)

The structure of the electric field can be interpreted as follow: the contribution of the charge density is dominant and this quantity is very sensitive to the variation of the current profile on the strap in the y-direction.

For example, the electric field structure of single resonant strap is, for x-component, dominated by the charge density and gives high amplitude of the x-component near the edges of the strap with an inversion at the middle of the strap; for y-component, the electric field associated to the charge density has two humps at the edges of the strap and goes slowly to an minimum value at the middle and the part associated to the j_y current shows only a component E_y with a wide hump centred on the strap.

The both contributions have the slightly the same amplitude but have opposite signs. We can notice that the z-component of the electric field is only due to the charge density. The density charge distribution gives a good idea of the near field in front of the ITER antenna.

The spatial dependencies of the current on the ITER antenna structure determine the main part of the topology of the near field.

To give a realistic map of the near field, the current distribution should be computed self-consistently as it is made in the ICANT code.

CONCLUSIONS

The ITER antenna computations seem to confirm the notion of the optimal density for the coupling ($5 \cdot 10^{19} \text{ m}^{-3}$ for $\nu = 55 \text{ MHz}$), which decreases with the frequency, and we have to check its evolution depends on the shape of the density profile.

The best coupling obtained is around 10 W/A per strap with a simplified ITER antenna lower than the expected value. This is perhaps due to a bad shape of the density profile at the edge.

It is well known that the RF sheath plays an important role on long pulse heating [5]. It is very important to minimise the rectified potential in dipole configuration therefore the parallel electric field E_z . The surrounding metallic wall contributes to reduce the component of the electric field at the edge of the box. The septa limit the charge density on the strap therefore the parallel electric field. The quasi-alignment of the screen blades with the magnetic field lines and the reduction of the open magnetic field lines contribute also to the minimisation of the rectified potential (geometry design). Another way is the reduction of the charge density on the antenna structure that is to say to have current profiles with low spatial gradients and higher coupling as possible.

The role of the oscillating charge density has to be study in more details (see the roles of the poloidal segmentation, real radiated power maximum around 4 segments as it is, and of the poloidal phasing) to know if it is possible to minimise its effects and to confirm in different other situations where a flat current profile is really better than a curved current profile.

To conclude the self-consistent determination of the current distribution is essential to obtain realistic near fields.

REPORTS AND PUBLICATIONS

- [1] S. Heuroux, S. Pécol "ICRH antenna coupling: near field computations" Annual report association EURATOM/CEA 2000 p 7-10.
- [2] S. Pécol, S. Heuroux, R. Koch and G. Leclert "Numerical modeling of the coupling of an ICRH antenna with a plasma with self-consistent antenna current" Computational Physics Communications (à paraître).
- [3] S. Pécol, S. Heuroux, R. Koch, G. Leclert, 27th EPS Conf. controlled fusion and plasma physics 12-16 June 2000 Budapest , ECA Vol. 24B (2000) 388-391.
- [4] D.W. Faulconer, J. Appl. Phys.**54**, 3810-3817 (1983).
- [5] M. Bécoulet, L. Colas, S. Pécol, J. Gunn, Ph. Ghendrih, A. Bécoulet, S. Heuroux "Edge plasma density convection during ICRH on Tore Supra" Phys. Plasmas (à paraître).

TASK LEADER

Stéphane HEURAUX

LPMIA UHP
 Faculté des Sciences Nancy I
 Boîte Postale 239
 54506 Vandoeuvre Cedex

Tél. : 33 3 83 91 25 72
 Fax : 33 1 83 27 34 98

E-mail : stephane.heuroux@lpmi.uhp-nancy.fr

TW1-TPH-ICRANT

Task Title : ICRF ANTENNA AND VACUUM TRANSMISSION LINE DEVELOPMENT

Design & manufacturing of a CW ICRF high power test rig and testing of next step antenna prototype components

INTRODUCTION

Although it is generally recognized that the principles of current Ion Cyclotron technology are applicable to Next Step devices, a number of key components, e.g. matching unit or vacuum window, require tests and qualification of presently foreseen design options.

Progress on these antenna and vacuum transmission line components issue requires the availability of a high power continuous wave (CW) ICRF test rig. The development of such a test rig is necessary to validate under fully representative conditions a number of next step antenna components. The test rig facility shall be able to set up a sufficiently high level of RF voltage (about 60 kV) and current (about 2 kA) under vacuum. It must be provided with pumping and water cooling, and equipped with all the measurements means required.

To begin with, a number of next step antenna possibly needed technology items are desirable to be tested on the ICRF test rig, including in particular sliding contact solutions.

2001 ACTIVITIES

The detailed design of a high power CW ICRF test rig was done. A general design view is given in figure 1.

The key idea –in order to carefully delimit the area where high RF voltages and currents are generated not to end with testing other components that the ones pursued- is to build up a T resonator. It would consist of :

- A T junction part (see figure 1), connected to the input power pressurised feed line through a short vacuum line, a Tore Supra type vacuum window, and a quarterwavelength stub (for the internal conductors cooling). An elbow is foreseen on one side to reduce the space requirements around the test rig.
- Short-circuited transmission line (not represented in FIG.1) at both end of the T junction, including on one side the prototype component to be tested. The lengths of these 2 parts will have to be such that the whole circuit is resonant (very little reflected power in the feed line).

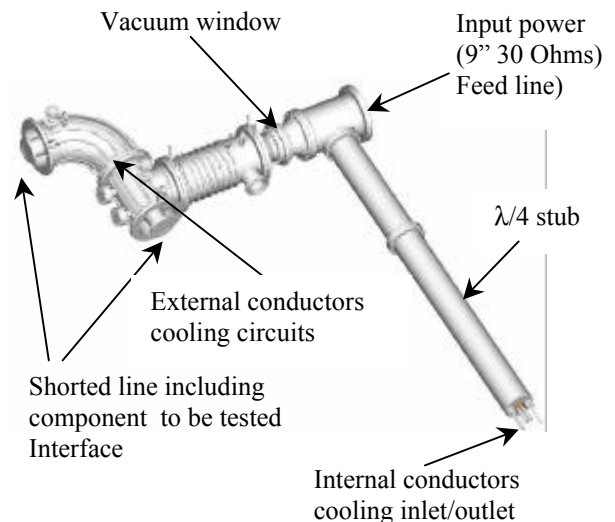


Figure 1 : Design view of the ICRF CW test rig

ELECTRICAL DESIGN

The T junction will be made of 9" 30 Ohms pieces of line. Outer diameter and characteristic impedance were chosen because there are representative of typical surrounding geometry of the components to be tested.

The operative frequency was chosen 58 MHz in order to cope to Tore Supra generator cavities pretuned frequencies.

Electrical computations were performed to assess several design RF issues. In particular, the effect of the surface material resistivity was investigated as low resistivity surface material (e.g. copper coating):

- allow to generate high RF voltage / current for a given input power,
- but make the resonant circuit very sensitive (high Q), and possibly hardly possible to tune.

A trade-off on the source power requirement (and cooling requirements, especially for inner conductors) vs matching sensitivity was found using partially all stainless steel parts and copper coated parts.

RF test specifications (60 kV, 2 kA) can be met with about 400 kW maximum of input power. The feeding line will then work at moderate current and voltage, without cooling required.

The baseline configuration of the test rig, which will be first qualified, features two short-circuited line module at both ends of the T junction. In order to cope with several uncertainties in the RF model (impedance jump due to change of diameter required at the interfaces for mechanical assembly, effect of line curvature in the elbow part, actual losses in the conductor and RF contact losses...), a final adjustment of the short-circuited line lengths at low power is foreseen.

The RF component testing could then be done by replacing one of the two short-circuited baseline module (RF current tests on the short end, and RF voltage standoff test on the long elbowed end)

MECHANICAL DESIGN, COOLING AND PUMPING

The water cooling of the test rig was designed taking into account the power density to be evacuated from the different parts.

- for the external conductors of the T junction, cooling tubes wined around and welded to the external surface of the conductors are foreseen. Finite Element thermal simulations were performed to assess the minimum distance between cooling tubes,
- for the internal conductors of the T junction, cooling chambers are foreseen.

Required rate of water flow and pressure drop in the cooling circuits were also estimated to design the hydraulic cooling network.

A pumping port will be provided in the vacuum feeding line section. Pumping time to achieved good vacuum level (around 10^{-6} mbar) has been estimated to a few hours with existing vacuum pumps.

CONCLUSIONS

The design of the CW ICRF test rig is completed according to the agreed requirements. Detailed manufacturing drawings of all parts of the test rig are available. Manufacturing is under way.

While waiting for the complete CW RF test rig to be fully manufactured, a first series of tests of one sliding contacts solution was performed on the present test stand. Multilam type RF contacts were used in fixed position. The aim of the test, namely 1 kARMS (i.e. 60 A/cm) RF carrying current under vacuum during 60 s was obtained without any visible degradation observed after dismounting the test set-up.

TASK LEADER

Sylvain BRÉMOND

DSM/DRFC
CEA Cadarache
13108 St Paul Lez Durance Cedex

Tél. : 33 4 42 25 76 41
Fax : 33 4 42 25 62 33

E-mail : sbremond@cea.fr

Task Title : NEUTRAL BEAM DEVELOPMENT FOR EDA EXTENSION EU-JA collaborative experiment on KAMABOKO source

INTRODUCTION

This work is carried out on the MANTIS test bed using the Kamaboko III negative ion source, which is a “model ITER source”, designed and supplied by JAERI, Japan. The ITER R&D task description states the objectives of this task as:

- a) To demonstrate the high performance H⁻/D⁻ ion production for long pulses, using the plasma grids developed for long pulse.
- b) To aim at higher current density ($\sim 300 \text{ A/m}^2$), at lower source filling pressure ($\sim 0.1 \text{ Pa}$).
- c) To develop long life cathodes for stable, reliable operation, and less frequent maintenance.

The difficulties encountered in obtaining reliable long pulse operation and the expected current densities at the anticipated power levels have meant that essentially all the work so far has been directed at objective a).

To reach the performance required by ITER, Cs has to be added to the plasma and the plasma grid has to operate at a high temperature of $\approx 300 \text{ }^\circ\text{C}$. Two long pulse plasma grids, designed and built by JAERI, have been successfully tested on MANTIS up to the expected operational arc power. The “frame cooled” grid support was damaged in transport from Japan, so the “actively cooled” grid has been used for the majority of the long pulse work.

Very reproducible arc discharges have been produced at the expected operational parameters, i.e. source filling pressure of 0.3 Pa , arc discharge power of $\approx 50 \text{ kW}$, with the plasma grid temperature constant at the design value of $\approx 300 \text{ }^\circ\text{C}$. Extraction and acceleration of H⁻ and D⁻ beams for 1000 s was achieved at the highest attainable arc power, $\approx 50 \text{ kW}$. Unfortunately the negative ion yield is only $\approx 40\%$ of that expected, for reasons as yet not understood, and the caesium consumption was found to be considerably higher than anticipated.

THE PRESENT STATUS IS :

The essential preparatory work and system modifications to allow long pulse operation, either at the expected parameters or above, was completed in 2000. In addition several diagnostics have been put in place which should allow a better understanding of the negative ion production to be reached, in particular a laser cavity ringdown system to measure the negative ion density a few millimetres in front of the plasma grid and a beam scanner to measure the beam profile (hence the accelerated H⁻/D⁻ uniformity). The status of the experiments is:

- Long pulses at the foreseen arc discharge power (Parc $\approx 50 \text{ kW}$) and filling pressure (0.3 Pa) have been regularly obtained.
- Extraction and acceleration for 1000 s has been demonstrated in hydrogen and deuterium operation.
- The plasma grid temperature (T_{pg}) is at, or close to, the "optimum" operating temperature, $>300^\circ\text{C}$ at the anticipated required power levels.
- At the discharge power (Parc) where the accelerated D⁻ current density was expected to be 200 A/m^2 , it is in fact only $\approx 80 \text{ A/m}^2$.
- The effect of varying the magnetic filter field from 850 to 1200 Gauss cm has been shown to have little effect on the negative ion yield.
- The caesium consumption during the long pulse experimental campaign was >500 times that expected.
- The laser cavity ringdown system could not be completely aligned due a geometric constraint within the source mounting flange.
- The signal observed by the beam scanner was too low to allow accurate beam profiles to be measured.

2001 ACTIVITIES

1000 s D⁻ AND H⁻ EXTRACTION AND ACCELERATION

Long pulse, 1000 s , operation with low source pressure ($\leq 0.3 \text{ Pa}$) and an accelerated D⁻ current density of 200 A/m^2 is required for ITER.

It has been found that the efficiency of production and extraction of D⁻ in an arc discharge can be substantially enhanced first by the addition of caesium, and then by operating with a hot plasma grid. Both these aspects are proposed for ITER and implemented in the KAMABOKO III source.

Negative ion yield

D⁻ and H⁻ beams have been extracted and accelerated for pulses of 1000 s duration under conditions that were expected to have yielded an H⁻ accelerated current density of 280 A/m^2 and a D⁻ current density of 200 A/m^2 , i.e. at an arc discharge power of $\approx 45 \text{ kW}$, a source filling pressure of 0.3 Pa , and with the plasma grid at $\approx 300^\circ\text{C}$ - see figure 1.

The negative ion yield deduced from the current drain of the high voltage (acceleration) power supply was 180 A/m² for H⁻ and 115 A/m² for D⁻, well below expectations.

The high voltage power supply current may include co-extracted and accelerated electrons, whereas it has been shown experimentally, and by calculation, that electrons cannot reach the calorimeter.

Therefore the calorimetrically determined value is the more certain. The calorimetrically determined current densities are 80 A/m² for D⁻ and 100 A/m² for H⁻.

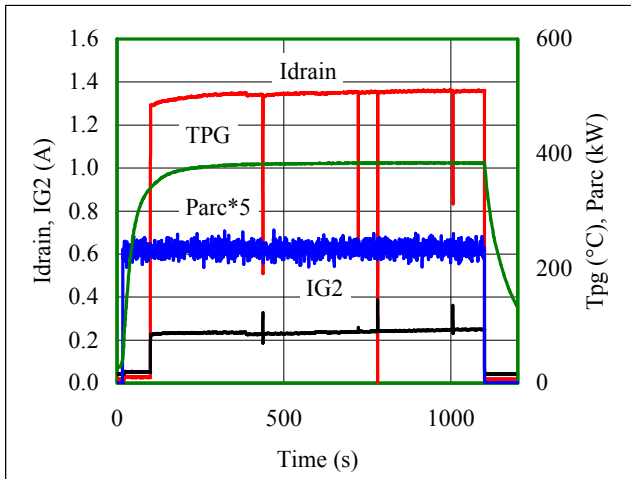


Figure 1a : 1000s H shot. Parc = 47 kW, extraction voltage = 6.5 kV, acceleration voltage = 25 kV - IG2 is the current to the extraction grid, which consists largely of electrons extracted from the source

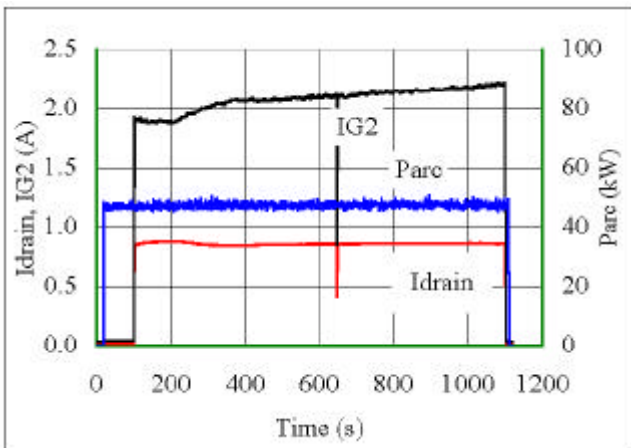


Figure 1b : 1000s D⁻ shot. Parc = 47 kW, extraction voltage = 6.5 kV, acceleration voltage = 25 kV - IG2 is the current to the extraction grid, which consists largely of electrons extracted from the source

Grid temperature effect :

The increase of negative ion yield with grid temperature seen during the long pulse operation of the KAMABOKO III ion source with the “frame cooled” (molybdenum) grid is ≤ 40 %, significantly below the > 100 % reported several times by JAERI - see figure 2. This explains, at least in part, the measured, low, D⁻ (or H⁻) yield.

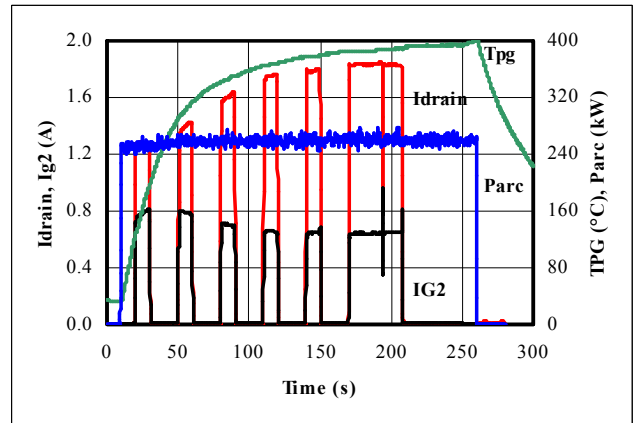


Figure 2 : The effect of the plasma grid temperature on the negative ion yield during long pulse operation is shown by the change in Idrain (The extraction/acceleration system was pulsed on and off during this pulse)

Beam optics and transmission

The transmission to the target, defined as the ratio of the calorimetrically determined current to the power supply drain current, was low, 48 % with H⁻ and 60 % with D⁻, whereas almost 100 % was expected. Beam profiles measured with an array of secondary emission probes behind the calorimeter profiles suggest a beamlet divergence of ≈ 4°, worse than expected, but not enough to explain the poor transmission.

Analysis of the aforementioned beam profiles indicates that 90 % of the beam power should have fallen on the calorimeter. This leads to the conclusion that the current density (referred to the plasma grid) was only 100 A/m² in H⁻, and 80 A/m² in D⁻.

When the accelerator was dismantled it was found that the “electron suppression grid” (ESG) was bowed, with the centre being 2 mm out of plane. This resulted in optics varying across the grid due to the varying acceleration gap and effective thickness of the extractor (ESG + extraction grid). This distortion also led to incorrect extraction and acceleration gaps being used as the ESG surface was taken as a reference during the installation of the grids.

Heating of the ESG, which would cause the observed distortion, can only occur by direct interception of accelerated particles.

Detailed calculations of electron, negative ion and back streaming positive ion trajectories have shown that this was probably due to negative ions when the extracted current density was ≈ 30 A/m² with an extraction voltage of 6 kV. This occurred in the initial phase of volume operation of the source; approximately 6 % of the H⁻ would have been intercepted by the ESG.

A new, single piece, all (electrodeposited) copper extraction grid was provided by JAERI and installed, with the correct extraction and acceleration gaps. This grid failed after a few shots with a water leak. Examination of the grid showed melting and delamination of the copper.

The size and location of the melted region corresponds well with the calculated high power density (530 W/cm^2) point arising from the extracted electrons. This design of grid has permanent magnets located just below the surface facing the extraction grid, with the $2.2 \times 2.2 \text{ mm}^2$ water-cooling channels behind the magnets. A careful assessment of the power and power density handling characteristics of the extraction grid is ongoing using the CASTEM 2000 3D code. Preliminary results indicate that the power handling threshold is below that required for full power operation, and that the threshold was reached during the experiments. (At full power operation the expected 200 A/m^2 of extracted electrons are accelerated onto the extraction grid with an energy of $\approx 10 \text{ keV}$.)

CAESIUM CONSUMPTION

At the beginning of the 1000 s shot campaign 5 g of Cs were introduced into the oven, and signs of Cs starvation were noted after a calculated 4.5 g had been bled into the source. Subsequently it has been confirmed that all the Cs had been used (the oven was empty).

Cs consumption rate

The total “arc only” and beam on periods during the 1000 s campaign on MANTIS were 43470 s and 21681 s respectively. As the accelerator on MANTIS has 49 apertures, the consumption on MANTIS per aperture per second, C_{MANTIS} was:

$$C_{\text{MANTIS}} = 1.56 \times 10^{-6} \text{ g/s per aperture}$$

The estimated the Cs consumption of the ITER source using the JAERI long pulse source data is:

$$C_{\text{ITER}} = 2.8 \times 10^{-9} \text{ g/s per aperture}$$

Thus the Cs consumption measured during the long pulse operation was **>500 times that expected on ITER**. It is hypothesised that this high consumption was due to a combination of increased loss during arc only operation and relatively high source wall temperatures, see following paragraph.

Cs⁺ loss in “arc only” operation

Neither extraction nor plasma grid bias voltages were during the arc only periods on MANTIS. Therefore Cs⁺ would have been free to escape from the source through the plasma grid, whereas during beam extraction it could not. It has been estimated that the Cs in the source plasma is more than 98% ionised, so the Cs flow (in the form of Cs⁰ and Cs⁺) from the source could be much greater than when the beam is extracted, when Cs⁺ is prevented from leaving the source. The Cs⁺ flow during arc only operation can be estimated assuming:

- The positive ion current is equal to the electron plus negative ion current.
- The negative ion current and electron current densities were 200 A/m^2 .
- The Cs⁺ current density is 1% of the H⁺ (or D⁺) current.

With these assumptions, the Cs⁺ current is 30 mA, and the flow is $4 \times 10^{-3} \text{ g/s}$. Thus in the of arc only operation, the amount of Cs that would have flowed into the accelerator is 1.7 g. This is a substantial fraction of the 5 g actually consumed, however it must be noted that there could be significant errors in this calculation as assumption b) is an upper limit, and the Cs⁺ current density in the plasma may be an underestimate as the Cs⁺ density in the plasma, hence the Cs⁺ current to the apertures in the plasma grid, will be a strong function of the Cs flux into the plasma, hence of the wall temperature (see following paragraph).

Increase in Cs loss due to “hot” walls

During long pulse operation ($>>10 \text{ s}$) the ion source reaches thermal equilibrium, and the inner surface of the source walls will be hotter than during short pulse operation. This would increase the vapour pressure of the Cs on the walls, increasing the Cs flow into the plasma. If it is assumed that the Cs and Cs⁺ densities in the source plasma are proportional to the Cs flow from the walls, the flow out of the source will be increased proportionately (both the Cs⁺ flow during arc only operation, and Cs⁰ at all times). A change in temperature from $30 \text{ }^\circ\text{C}$ to $70 \text{ }^\circ\text{C}$ causes the vapour pressure to increase by ≈ 30 . (The temperature of the inside surface of the source is likely to change over this range in passing from short to long pulse operation.)

DISCUSSION/CONCLUSION

Negative ion yield

D⁻ has been extracted and accelerated from the KAMABOKO III negative ion source for 1000 s at the expected operating conditions of the ITER FEAT source, but the accelerated D⁻ current density is found to be significantly below that required for ITER FEAT at 80 A/m^2 compared with 250 A/m^2 .

This is partly explained by the fact that the increase in negative ion yield as the plasma grid temperature is increased is significantly below that measured during short pulse operation in Japan. Since the enhancement of the negative ion yield is supposed to be due to the creation of the optimum Cs layer thickness on the grid, it is suggested that the reduced effect observed in long pulses may have been due to a misbalance between the Cs flux to the grid and the grid temperature. As the thickness is determined by a balance between Cs flow to the grid, and evaporation from it, the increased Cs flow obtained during long pulse operation (see paragraph before) would alter this balance, and the optimum temperature could be $>>300 \text{ }^\circ\text{C}$.

Cs consumption

As explained in paragraphs before, an increase in Cs consumption is to be expected from both the hotter source walls, and from the loss of Cs⁺ through the plasma grid during arc only operation.

If it is assumed that the Cs density in the source plasma is proportional to the Cs flow from the walls, the hotter walls alone cannot explain the >500 times higher flow observed on MANTIS than expected for ITER.

Cs^+ can be lost through the plasma grid if no extraction voltage is applied, and if no bias is applied between the plasma grid and the source plasma, which was the case during arc only operation during this campaign. Long periods of arc only operation were used to ensure that the plasma grid reached its steady state temperature, hence that the negative ion yield would be constant for the rest of the pulse. During beam operation, the plasma grid is normally biased positive with respect to the anode, therefore the plasma, which would inhibit the Cs^+ flow to the grid, and the Cs^+ flow out of the source. It is suggested that early application of the grid bias could substantially reduce the Cs consumption. Also, application of the (negative ion) extraction voltage prevents the flow of Cs^+ from the source, so that early application of the extraction voltage (not necessarily of the acceleration voltage) could be also considered.

The variation in the vapour pressure of Cs over the possible range of wall temperatures is important, and JAERI have already demonstrated that having a higher temperature coolant (with a consequent increase in the wall temperature) significantly increases the Cs consumption. Hence it is evident that the cooling of the ITER ion source is important. It is suggested that a section of the ITER source wall should have a separate cooling loop, perhaps with the capacity to vary the temperature.

REPORTS AND PUBLICATIONS

D Boilson, H P L de Esch, R S Hemsworth, M Kashiwagi, P Massmann and L Svensson, RSI 73, 2 (2002).

Filter variation and long pulse operation of the KAMABOKO III source on the MANTIS test bed. L Svensson, D Boilson, H P L de Esch, R S Hemsworth, M Kashiwagi and P Massmann. Meeting of the co-ordination Committee for Neutral Beams, Cadarache France 14/15 April 2001.

Magnetic filter variation study on the KAMABOKO III source. L Svensson, D Boilson, H P L de Esch, R S Hemsworth and P Massmann. ITER review meeting, Naka Japan, 28-31 May 2001.

Filter Variation and Long Pulse Operation of the KAMABOKO III source on the MANTIS test bed. L Svensson, D Boilson, H P L de Esch, R S Hemsworth, M Kashiwagi, and P Massmann. Neutral Beam Development for EDA Extension, R&D TASK T512 Final report.

TASK LEADER

D. BOILSON

DSM/DRFC/SCCP
CEA Cadarache
13108 St Paul Lez Durance Cedex

Tél. : 33 4 42 25 62 41
Fax : 33 4 42 25 62 33

E-mail : boilson@drfc.cad.cea.fr

Task Title : TRANSPARENT POLYCRYSTALLINE WINDOWS

INTRODUCTION

Polycrystalline Yttrium Oxide (Y_2O_3) is an alternative candidate to magnesium spinel ($MgAl_2O_4$) since it can be used to fabricate transparent plates for windows, with a wide optical transmission range from 0.25 to 9.5 μm . In addition to optical properties, Yttrium oxide is a refractory material that can be used above 1200°C with good mechanical properties.

Worked performed at CEA in 2000, aimed at improving the transparency of polycrystalline Y_2O_3 specimens. A process was worked out to introduce the doping content, and the influence of the sintering conditions was investigated.

During the first semester 2001, CEA aimed at measuring mechanical and optical properties. Thermal shocks were performed on transparent samples and influence of those tests on optical transmission of Y_2O_3 is reported. During the second semester 2001, samples have been delivered to DRFC for specific tests.

2001 ACTIVITIES

MECHANICAL PROPERTIES

Hardness measurement

Hardness was measured using a Wolpert equipment with a V-testor 4021. A pyramidal diamond of high quality, with a surface angle equal to 186°, is used to penetrate the material. Energy of penetration is given using a calibrated load on top of the diamond. The print resulting from diamond penetration is a square. Hardness can be calculated from the dimension of this square print.

$$H_v = P/\alpha_0 a^2$$

with : P : load (kg)
 a : 1/2 diagonal of the square print
 α_0 : 2 (constant data given in literature)
 H_v : hardness ($kg \cdot mm^{-2}$)

While the diamond stays on the material, part of the stress due to penetration can be relaxed so it is important to keep this parameter constant since it has some influence on the size of the square print and related hardness data. For those tests, diamond stays for 15 seconds on the surface.

Hardness is intrinsic characteristic of the material that should not depend on the load but those penetration tests show a sensible influence of H_v with the load P; The higher the load, the larger the print the more accurate the data should be.

Based on this experimental results, we evaluate the hardness of polycrystalline Y_2O_3 equal to 720 $kg \cdot mm^{-2}$. These data is close to data found in literature. D.C. Harris [1] finds hardness equal to $720 \pm 30 \text{ kg} \cdot mm^{-2}$. Also J.Montintin [2] show that hardness decreases when grain size and/or porosity increases.

Toughness

Toughness is the ability of a material to withstand the fast propagation of a crack. It is calculated from the dimension of cracks resulting from Vickers indentation. The equation used to calculate toughness is :

$$K_{Ic} = \delta / (H_v \cdot c^{3/2}) \sqrt{(E \cdot P)}$$

with : δ constant data equal to 0.016
 E Young's modulus = 170 GPa
 P load used for penetration (N)
 H_v Vicker's hardness (GPa)
 C : 1/2 crack length (mm)

The average data resulting from those measurements is $1.6 \pm 0.2 \text{ MPa m}^{1/2}$

This technique is difficult to use since it is quite difficult to make accurate measurement of the crack length. While the material is relaxing, crack is still propagating for some time after penetration. It tends to lower the data for toughness. The results presented above must be used as estimated data. In the literature, toughness is $1.8 \text{ MPa m}^{1/2}$ for this material.

Bending strength

3 point bending tests are performed on square rods of transparent polycrystalline Y_2O_3 . The ultimate strength (σ_f) is calculated from the following equation :

$$\sigma_f = (3 \cdot P \cdot c) / (2 \cdot a \cdot b^2)$$

with : a = sample width (mm)
 b = sample thickness (mm)
 P = breaking load (N)
 c = distance between holding points (mm)

Span distance is equal to 20 mm. This data is kept unchanged during the test. The average data resulting from those measurements is $\sigma_f = 149 \pm 22 \text{ MPa}$.

Those results are quite low compared to data found in the literature [1]. For yttrium oxide fabricated by hot isostatic pressing, ultimate bending strength is usually around 215 MPa when the test speed is equal to 0.5 mm/min.

The difference in bending strength can be explained by the lower speed used in those tests (0.2 mm/min).

Results can also be compared to those we obtained for polycrystalline magnesium spinel (220 MPa) under the same experimental conditions (0.2 mm/min).

If yttrium oxide can be interesting for its transmission range it is less interesting than transparent magnesium spinel for structural application.

Weibull modulus (m)

Weibull modulus shows the structural homogeneity of the material. It is a statistical data that express the level of reproducibility for microstructural characteristics of the material. It is also related to statistical distribution of the size of defects.

One calculates Weibull modulus from data obtained from 3 pt bending test. Probability (P_i) for a sample to break under a stress σ_i is given by the following equation :

$$P_i = [i-(3/8)]/[N+(1/4)]$$

with i = serial number for the 3 pt bending test
 N = amount of measurements performed for the 3 pt bending test.

Weibull modulus is estimated around 7 MPa. Such data is related to a material having defects homogeneously distributed in the material.

OPTICAL PROPERTIES AFTER THERMAL SHOCKS

3 types of tests are performed on disks :

- 1st type (hot to RTW) : sample is heated up to 300°C before to be thrown in cold water (15°C). Sample is maintained in water for 1 minute.
- 2nd type (hot to LN) : sample is heated up to 300°C before to be thrown in liquid nitrogen. Sample is maintained in nitrogen for 1 minute.
- 3rd type : (RT to LN) sample at room temperature is thrown in liquid nitrogen. Sample is kept for 1 minute in nitrogen.

Optical transmission is measured on each disk before and after the thermal shock, to quantify the influence of thermal shock on optical properties of the polycrystalline Y_2O_3 material.

a/ 1st type : “hot to RTW”

After the test, the disk made of transparent polycrystalline Y_2O_3 shows a network of cracks.

Those cracks are starting from the outside perimeter of the disk. Since the peripheral surface of the disk is not polished, each roughness is a weak point of the structure and a possible starting point of a crack.

Optical measurement is performed after each test to see the evolution of the crack network.

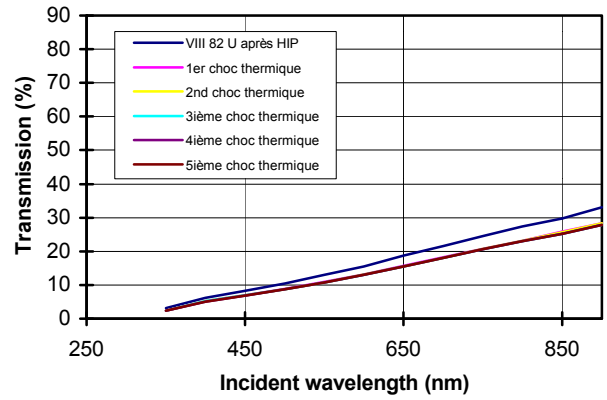


Figure 1 : Optical transmission of polycrystalline Y_2O_3 in UV-Visible range after “hot to RTW” thermal shock

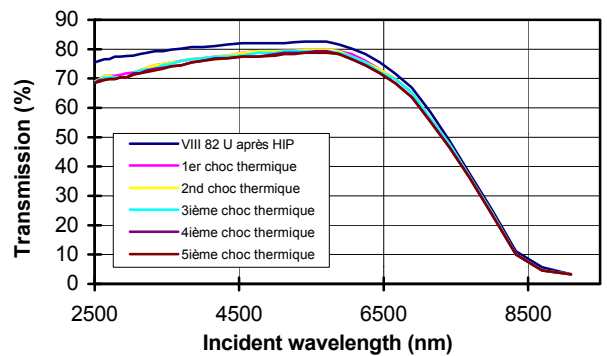


Figure 2 : Optical transmission of polycrystalline Y_2O_3 in IR range after “hot to RTW” thermal shock

- When a sample of transparent polycrystalline Y_2O_3 heated at 300°C is thrown in water at Room Temperature, cracks initiate from the unpolished outer surface. Optical transmission decreases, both in UV and IR range, due to diffusion of light on the cracks.
- Cut-on and cut-off data stay unchanged.
- The degradation of optical transmission is not amplified by additional thermal shocks.



Photo 1 : Y_2O_3 disk brazed on titanium

b/ 2nd type : “hot to LNT”

The variation of temperature for this test is much larger than in the previous test. For the first test, variation of temperature applied to the sample, was about 275°C. It is 510°C for the second test. We expect a stronger effect and higher degradation of the material.

Actually, the degradation observed is less severe than for the first test. The crack network is reduced. This result can be explained by evaporation of liquid nitrogen on the surface of the hot sample. Heat exchange is slower for a solid in gas surrounding than when it is immersed in a liquid.

- After the thermal shock, the optical transmission decreases in the UV-visible range. The difference does not exceed 4 %.
- After thermal shock there is no significant modification of optical transmission in IR range.
- As we observed in previous test, there is no more degradation of the material than after the first test, when samples is shocked several times.

c/ 3rd type : “from RT to LNT”

This third test is less severe than the previous one since the ΔT is 235°C from room temperature to liquid nitrogen. Sample submitted to this test shows only few cracks throughout the material. Sample seem to be less damaged than in previous tests.

Optical transmission measurements show no degradation of the transparent polycrystalline Y_2O_3 material when immersed from room temperature to liquid nitrogen, neither in UV nor in IR range.

Observation of few cracks means there is probably a mechanical degradation of the material.

CONCLUSION

The mechanical characterizations show that Y_2O_3 is not as performing for structural application than magnesium spinel ($MgAl_2O_4$) in particular due to its lower bending strength.

Thermal shock tests show that material is damaged. Cracks could be reduced by polishing the edge of the disks to reduce structural defects on the outer surface. Cracks are decreasing the optical transmission. Additional shock have negligible effect on transmission properties.

Samples (photo 1) have been delivered to DRFC. It will allow to perform specific test like post irradiation characterization to complete data available on this material and help to evaluate its potential for application in Fusion reactor.

REFERENCES

- [1] Daniel C.Harris, George A.Hayes, Nancy A.Jaeger, “Mechanical strength of hemispheric domes of yttria and lanthana doped yttria”, *J.Am.Ceramic.Soc.*, 75 [5]1247-53 (1992).
- [2] J.Montintin « Etude de céramiques élaborées par compression isostatique à chaud. Relation entre microstructure et propriété. » Thèse de l’Université de Limoges 1991.

REPORTS AND PUBLICATIONS

N.Lochet. Study of thermo mechanical properties of Y_2O_3 material. Report CEA/DRT/DECS/SE2M/LECMA 01-DT-13 – 25/06/2001.

N.Lochet. Study of thermo mechanical properties of Y_2O_3 material. Report CEA/DRT/DECS/SE2M/LECMA 01-DT-027 – 19/11/2001.

TASK LEADER

Nicolas LOCHET

DRT/DECS/SE2M/LECMA
CEA Saclay
91191 Gif-sur-Yvette Cedex

Tél. : 33 1 69 08 32 16
Fax : 33 1 69 08 57 54

E-mail : nicolas.lochet@cea.fr